# Comparing Observations and Simulations of the Streamwise Vorticity Current and the Forward-Flank Convergence Boundary in a Supercell Storm

ALEX SCHUETH,[a] CHRISTOPHER WEISS,[a] AND JOHANNES M. L. DAHL[a]

[a] *Atmospheric Science Group, Department of Geosciences, Texas Tech University, Lubbock, Texas*

(Manuscript received 31 July 2020, in final form 22 February 2021)

ABSTRACT: The forward-flank convergence boundary (FFCB) in supercells has been well documented in many observational and modeling studies. It is theorized that the FFCB is a focal point for the baroclinic generation of vorticity. This vorticity is generally horizontal and streamwise in nature, which can then be tilted and converted to midlevel (3–6 km AGL) vertical vorticity. Previous modeling studies of supercells often show horizontal streamwise vorticity present behind the FFCB, with higher-resolution simulations resolving larger magnitudes of horizontal vorticity. Recently, studies have shown a particularly strong realization of this vorticity called the streamwise vorticity current (SVC). In this study, a tornadic supercell is simulated with the Bryan Cloud Model at 125-m horizontal grid spacing, and a coherent SVC is shown to be present. Simulated range–height indicator (RHI) data show the strongest horizontal vorticity is located on the periphery of a steady-state Kelvin–Helmholtz billow in the FFCB head. Additionally, a similar structure is found in two separate observed cases with the Texas Tech University Ka-band (TTUKa) mobile radar RHIs. Analyzing vorticity budgets for parcels in the vicinity of the FFCB head in the simulation, stretching of vorticity is the primary contributor to the strong streamwise vorticity, while baroclinic generation of vorticity plays a smaller role.

SIGNIFICANCE STATEMENT: Supercell storms (long-lived thunderstorms with rotating updrafts) are responsible for producing most tornadoes, especially strong tornadoes. More than 50 years of research has been devoted to understanding how supercells work and the processes that lead to tornado formation. Recent computer simulations of tornadic supercells have shown a localized region of rotation [called the streamwise vorticity current (SVC)] feeding into the storm at low levels that could amplify rotation near the surface into a tornado. This study simulates the SVC in order to better understand the origin and dynamics associated with it. We also compare the simulation to high-resolution mobile radar observations to confirm that the SVC exists in real supercells.

KEYWORDS: Cold pools; Density currents; Kelvin-Helmholtz instabilities; Supercells; Vorticity; Radars/Radar observations

## 1. Introduction

Streamwise vorticity is known to be the fundamental source of rotation in updrafts (Davies-Jones 1984; Dahl 2017), and ambient streamwise vorticity has been shown to be a useful environmental parameter for supercell and tornado forecasting (Davies-Jones 1984; Davies-Jones et al. 1990; Davies-Jones and Brooks 1993; Droegemeier et al. 1993; Johns et al. 1993; Coffer and Parker 2017; Coffer et al. 2017; Coffer and Parker 2018). However, baroclinically generated vorticity can augment environmental vorticity and contribute significantly to the strength of the low-level mesocyclone. Precipitation in supercells can introduce dense air near the surface through evaporation and melting of hydrometeors, as well as the density of the precipitation itself. Cold pool strength (density surplus) can be modulated by factors including (e.g., microphysics forcing [Dawson et al. 2010; Mallinson and Lasher-Trapp 2019], aerosol concentration [Gilmore et al. 2004; Lerach and Cotton 2012] and subcloud relative humidity [Markowski et al. 2002; Brown and Nowotarski 2019]). Gust fronts exist on the periphery of strong cold pools, and are characterized by abrupt wind shifts, a nonhydrostatic pressure jump, and a strong density gradient. The density gradient across the sloped head of the gust front can be a source for baroclinic vorticity generation, and thus pertinent to supercell evolution.

### a. Storm-scale simulations

To further understand the characteristics of supercell generated cold pools and associated outlays of near-surface thermodynamic boundaries, multiple computer simulations have been conducted. Klemp and Rotunno (1983) simulated a supercell with a horizontal grid spacing of 1 km, and identified a rear-flank gust front (RFGF) on the eastern edge of the rear-flank downdraft (RFD) cold pool. As their storm evolved, the forward-flank gust front (FFGF) formed in the vicinity of the forward-flank reflectivity gradient (FFRG). In the region immediately behind this boundary, the flow was nearly parallel to the boundary, generating horizontal baroclinic vorticity along the trajectories of inflow parcels. As the flow reached the updraft, the baroclinically generated vorticity augmented the mesocyclone.

Beck and Weiss (2013) simulated a supercell with 250-m horizontal grid spacing and found three primary storm-scale

Denotes content that is immediately available upon publication as open access.

*Corresponding author*: Alex Schueth, alex.schueth@ttu.edu

DOI: 10.1175/MWR-D-20-0251.1

boundaries. The RFGF formed first, followed by multiple transient left-flank convergence boundaries (LFCB), due to surges in the left-flank downdraft (LFD, northwest of the updraft), that eventually consolidated into a single LFCB. Slowly throughout the simulation, a forward-flank convergence boundary (FFCB) formed in the vicinity of the FFRG, which started as a very weak convergence boundary that intensified with time. The use of ''convergence boundary'' was preferred over ''gust front'' due to the lack of a hydrostatic pressure gradient or pronounced wind shift across the boundary. Streamwise vorticity was found to be present along the FFCB and LFCBs with a typical magnitude of $0.04\,s^{-1}$. This vorticity was an order of magnitude larger than the environmental vorticity, and parcel trajectories confirmed the residence time in the baroclinic zone was favorable for significant solenoidal vorticity generation. Markowski et al. (2014), Dahl et al. (2014), and Dahl (2015) also found a band of concentrated vertical vorticity near the surface in a similar storm-relative placement and orientation to the LFCB described by Beck and Weiss (2013), which was attached to the tornado-like vortices in their simulations.

Orf et al. (2017, hereafter ORF17) simulated a supercell at an extremely high resolution (30-m isotropic grid spacing) and were able to model the entire life cycle of a long-lived EF5 tornado. It was observed that a feature, dubbed the streamwise vorticity current (SVC), preceded tornadogenesis and was correlated with its demise. The SVC was described as a persistent ''tube'' of streamwise vorticity located immediately on the cool side of the boundary the authors identified as the forward-flank downdraft boundary. It is located in a baroclinic zone where horizontal vorticity can be generated baroclinically and rises steadily as it approaches the updraft, before being abruptly tilted and stretched at the base of the updraft. Many other simulations have noted a focused area of baroclinically enhanced streamwise vorticity entering the mesocyclone at low levels from the north and east (e.g., Klemp and Rotunno 1983; Rotunno and Klemp 1985; Wicker and Wilhelmson 1995; Adlerman et al. 1999; Beck and Weiss 2013; Tanamachi et al. 2013). However, none of those simulations were at a small-enough grid spacing (Bryan et al. 2003) to be able to resolve storm-scale eddies and thermodynamic gradients near boundaries that allow streamwise vorticity to manifest itself as a coherent horizontal vortex.

### b. *Storm-scale observations*

While the SVC has not been the specific focus of observation in a field campaign, several studies have inadvertently observed features with similar attributes to the SVC. A dual-Doppler synthesis made by Dowell and Bluestein (1997) of the 17 May 1981 Arcadia, Oklahoma, tornadic supercell was the first observational study that alluded to the existence of the SVC. In the synthesis, the parcels feeding the low-level mesocyclone were found to originate from the east, and later from the northeast, parallel to the FFRG and along an inferred baroclinic boundary. However, the analysis was too coarse to resolve subkilometer scale features near the surface, like the SVC. Dowell and Bluestein (2002a,b) used airborne dual-Doppler radar as well as mobile mesonets to sample a tornadic supercell near McLean, Texas, on 8 June 1995. Despite the airborne dual-Doppler coverage only extending down to around 500 m AGL, multiple kinematic boundaries were observed within the forward flank. Additionally, the placement and orientation of vertical vorticity maxima were consistent with horizontal streamwise vorticity along a boundary in the forward flank being tilted into the vertical. Dual-Doppler analysis from Kosiba et al. (2013) on the Goshen County, Wyoming, storm on 5 June 2009 revealed that backward-integrated parcels from the low-level mesocyclone generally originated along or just north of the kinematically identified FFCB. Most of the parcels that were backward integrated went below the data horizon implying a lower source region that could not be identified; however, those that remained in the analysis domain originated around 300 m AGL. Mobile mesonets on the Goshen County, Wyoming storm that transected the FFCB found a baroclinic zone present and dual-Doppler analyses confirmed enhanced horizontal vorticity along the boundary consistent with baroclinically generated vorticity. Assimilating these data into a supercell simulation using an ensemble Kalman filter technique, Marquis et al. (2016) corroborated the findings from Kosiba et al. (2013) and further showed that the baroclinically generated horizontal vorticity magnitude was associated with tornado intensity.

Many studies have observed a kinematic boundary in the forward flank (akin to the FFCB) using single-Doppler radar analysis (Wakimoto and Liu 1998; Wurman et al. 2007; Romine et al. 2008; Frame et al. 2009; Kosiba et al. 2013). Other studies have shown that, in some supercells, thermodynamic boundaries exist near the FFRG (Shabbott and Markowski 2006; Skinner et al. 2011; Kosiba et al. 2013; Skinner et al. 2014; Weiss et al. 2015). However, the magnitudes of the horizontal density gradients across thermodynamic boundaries near the FFRG can vary widely. Some of the supercells sampled by Shabbott and Markowski (2006) did not contain a strong thermodynamic boundary along the periphery of the forward-flank cold pool, but rather a broad baroclinic zone. In their study, the storms that did contain a strong thermodynamic boundary were generally nontornadic with excessive virtual potential temperature deficits in the downdraft. The authors estimated that despite $0.005–0.02\,s^{-1}$ of baroclinically produced vorticity accumulated over a 5-km distance, the air lacked enough buoyancy for the vorticity to be adequately tilted and stretched in the updraft, and thus was not realized by the storm. All of the aforementioned studies did contain a much stronger cold pool behind (northwest of) the left-flank boundary (compared to the forward-flank inflow modification and RFD), typically extending north or a bit northwest of the mesocyclone center. This colder cold pool also typically had a stronger thermodynamic gradient, separating low-$\theta_e$ air from more buoyant air to the east, similar to the three boundary model presented by Beck and Weiss (2013).

To summarize, past numerical simulations have identified regions of strong streamwise vorticity associated with forward-flank baroclinic boundaries. However, few observational studies have been able to identify these boundaries and none have been able to convincingly demonstrate the existence of strong coherent streamwise vorticity in this region. Therefore, this study aims to

investigate if the SVC exists and is an observable feature using high-resolution radar observations, and to further our understanding of its structure, and the forcings that lead to its formation and maintenance using an idealized cloud model. It is hypothesized that parcels will flow along the baroclinic boundary, accumulating substantial baroclinically generated vorticity while being horizontally stretched. Once the parcels reach the base of the updraft, they are still positively buoyant enough to rise and can contribute to the low-level mesocyclone. Specifically, the research questions in this study are:

1) What are the main physical characteristics (position, orientation, and structure) of the SVC?
2) What are the forcing mechanisms driving the SVC?
3) Do high-resolution radar observations confirm the presence of the SVC, and do these observations compare well with the simulations?

## 2. Methodology

### a. CM1 configuration

Scientists from several universities and the National Severe Storms Laboratory (NSSL) collaborated for a small, mobile field project called the Rivers of Vorticity in Supercells (RiVorS) from 20 May to 13 June 2017. A sounding launched in the preconvective environment near Cheyenne, Wyoming, on 12 June 2017, where multiple tornadic supercells developed, served as the base state for the simulation used in this study (Fig. 1). The winds in the observed sounding were modified between 0 and 1 km AGL to better match High-Resolution Rapid Refresh (HRRR) soundings of the environment. Additionally, the temperature profile was increased by about 2 K in the lowest 3 km to remove a small inversion and retain a constant lapse rate.

Version 19.5 of the Bryan Cloud Model (CM1; Bryan and Fritsch 2002) was used for this three-dimensional (3D) idealized simulation. The specifications of the model design are shown in Table 1. To initiate a strong, isolated, and sustained supercell thunderstorm in the environment discussed above, the updraft nudging technique is adapted from Naylor and Gilmore (2012) with slightly modified parameters. The ellipsoidal vertical velocity perturbation is located 1500 m above the surface with a 7500-m horizontal radius and a 1500-m vertical radius. The maximum vertical velocity is 13 m s$^{-1}$ until $t = 1500$ s before ramping down to zero by $t = 1800$ s. To adequately resolve the SVC, a horizontal grid spacing of 125 m is used, which is consistent with the $O(100)$-m recommendation made by Bryan et al. (2003) to properly resolve turbulent structures. The grid is translated at a constant $(u, v) = (10.5, 8.7)$ m s$^{-1}$ to account for right-moving storm motion.

### b. Parcel setup

Parcels are used in this simulation to investigate trajectories through the SVC. Vorticity budgets are calculated to quantify the different sources of vorticity along the each parcel trajectory. The vector vorticity equation is

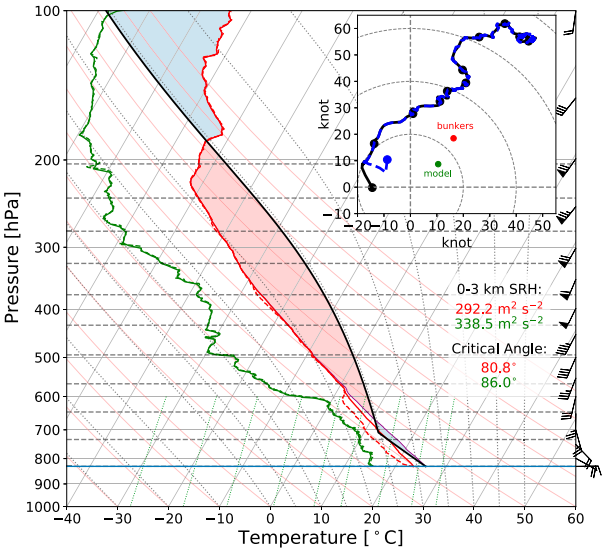


FIG. 1. Skew $T$–log$p$ diagram of NSSL's Probe 1 observed sounding east of Cheyenne, WY, in the preconvective environment at 1930 UTC 12 Jun 2017. The observed temperature and dewpoint traces are dashed red and green lines, respectively, and the observed wind profile is a dashed blue line on the hodograph. The modified sounding that was used as the CM1 base-state is depicted in solid lines on the skew $T$–log$p$ (red and green) and hodograph (black). The virtual temperature profile is in purple. The red dot on the hodograph indicates storm motion calculated by the method of Bunkers et al. (2000), and the green dot indicates the CM1 grid motion to keep the storm centered. The black dots on the hodograph as well as dashed horizontal gray lines on the skew $T$–log$p$ diagram represent 1-km height increments up to 10 km.

$$\frac{D\boldsymbol{\omega}}{Dt} = (\boldsymbol{\omega}\cdot\nabla)\mathbf{V} - (\nabla\cdot\mathbf{V})\boldsymbol{\omega} + \frac{\nabla\rho\times\nabla p}{\rho^2} + \nabla\times F_{\mathrm{fr}}, \qquad (1)$$

where $\boldsymbol{\omega}$ is the vorticity vector, $\mathbf{V}$ is the velocity vector, $\rho$ is air density, $p$ is air pressure, and $F_{\mathrm{fr}}$ is the frictional force. The first two terms on the right-hand side of (1) are classically described as the tilting and stretching terms. Despite tilting being undefined for 3D vorticity, the tilting term inherently contains vorticity stretching (Davies-Jones 1982; Dahl et al. 2014), and thus is combined with the stretching term and referred to as such. The third term is baroclinic vorticity generation, and the final term includes implicit (numerical) mixing as well as the effect of the subgrid-scale (SGS) turbulence closure. The parcels are forward integrated in the model using the RK2 scheme (Wicker and Skamarock 2002) and averaged winds to mitigate the effect of acoustic waves. The vorticity tendencies are calculated for each grid point and then trilinearly interpolated to the parcel location at each model time step.[1] These five vorticity tendencies make up the entire vorticity budget and have

[1] Further details on the methods are described in Boyer and Dahl (2020).

TABLE 1. Model configuration.

| Parameter | Description |
|---|---|
| Model | CM1 version 19.5 |
| Horizontal grid spacing | 125 m constant |
| Vertical grid spacing | 25 m below 3 km AGL, stretched to 125 m at 15 km AGL |
| Domain extent | 144 km × 144 km × 18 km |
| Numerics | RK2 (Wicker and Skamarock 2002), fifth-order advection |
| Microphysics | Morrison et al. (2009) double-moment |
| Turbulence closure | Smagorinsky (1963) |
| Cloud forcing | Updraft nudging (Naylor and Gilmore 2012) |
| Pressure solver | Klemp–Wilhelmson time splitting, vertically implicit |
| Lateral boundary conditions | Open radiative |
| Top and bottom boundary conditions | Free slip |

been custom added into CM1 as output for each parcel at each model time step. The model vorticity field is trilinearly interpolated to the parcel location and compared to the results of the integrated budgets.

### c. RHIs

Since the SVC has been previously identified as a horizontal vortex, classic plan position indicator (PPI) radar scanning strategies are poorly equipped to detect such a feature. This is perhaps one of the reasons why the SVC apparently has not been directly observed in Doppler radar data (Dixon et al. 2018). To better detect the SVC, an RHI scan whose azimuth is normal to the axis of the SVC is desired. Since the SVC forms along the FFCB, the axis of the horizontal vortex and the orientation of the FFCB should be roughly parallel. If the RHI azimuth is not perpendicular to the FFCB, the radial velocity representation of the SVC will be skewed such that the vortex will appear to be stretched radially. This parallax error is negligible for small angles but increases as the angle between the azimuth of the RHI and the FFCB deviates from orthogonal.

To compare the model to any observations, simulated RHIs are constructed, consistent with the Texas Tech University Ka-band (TTUKa) mobile radar specifications stated by Weiss et al. (2009) with an updated half-power beamwidth of 0.33°. The average maximum unambiguous range is approximately 13 km based on the pulse repetition frequency used in RiVoRS. There are 67 elevation angles from 0.3° to 20.1° (every 0.3°) and each ray contains 1000 equally spaced bins. Since each bin is approximately 15 m long, the simulated RHI vastly oversamples the model data. At each bin along each ray, the 3D simulated dataset is cubic spline interpolated to that RHI bin.

The radial velocity field ($V_r$) can be found by converting the ground-relative wind vectors in Cartesian coordinates ($u$, $v$, $w$) to spherical coordinates [Weisstein 2020, their Eq. (19)] using (2), where $\psi$ is the azimuth angle and $\phi$ is the elevation angle of the ray:

$$V_r = u\cos(\psi)\sin(90°-\phi) + v\sin(\psi)\sin(90°-\phi) + w\cos(90°-\phi). \quad (2)$$

To foster a better comparison between the simulated RHIs and the TTUKa observed RHIs, it is desirable to infer vorticity from the radial velocity field. The definition of vorticity in spherical coordinates [Weisstein (2020), their Eq. (89)] is manipulated such that

$$\nabla \times \mathbf{V} \approx \frac{1}{r}\frac{\partial V_r}{\partial \phi}\hat{\boldsymbol{\psi}}, \quad (3)$$

where $\mathbf{V}$ is the velocity field, $\hat{\boldsymbol{\psi}}$ is the azimuthal unit vector, and $r$ is radius from the origin (radar). The radial gradients of meridional velocity are much weaker than the meridional gradients of radial velocity, and thus the $(\partial/\partial r)(rV_\phi)$ term is neglected in (3).

## 3. Modeled FFCB structure

### a. Storm evolution

At $t$ = 3600 s in the simulation, the storm began to show supercellular characteristics including a persistent mesocyclone, a radar reflectivity hook echo, and distinct cold pools in the forward flank and the left flank (Fig. 2a). Three main thermodynamic boundaries, intersecting at a "triple point" beneath the low-level updraft, are present at this time: the RFGF extending south of the triple point, the weak FFCB extending northeast of the triple point, and the LFCB extending west-northwest of the triple point, similar to that found by Beck and Weiss (2013). The triple point is the intersection of the RFGF, the FFCB, and the LFCB (when applicable) and is generally where the maximum surface convergence occurs, and thus is also the position of the low-level updraft.

The left-flank cold pool is generated from the primary downdraft that began shortly after storm initiation. The boundary on the eastern edge of this cold pool is categorized as the LFCB and RFGF, to the north and south of the triple point, respectively (Fig. 3a). Between $t$ = 3600 and 6000 s, the LFCB slowly rotates counterclockwise and away from the triple point, such that, after $t$ = 6000 s, it has weakened considerably and exited the storm to the west (Figs. 2a–e). At $t$ = 6600 s, cold ($\theta_e' < -16$ K), negatively buoyant downbursts [similar to those found by Beck and Weiss (2013)] west and northwest of the triple point begin to create new thermodynamic boundaries (Figs. 3f–i). By 9000 s, a broader, weaker, negatively buoyant downdraft ($\theta_e' \sim -8$ K) creates a secondary LFCB closer to the FFCB (Figs. 3j–l).

While the RFD cold pool was the same as the LFD cold pool initially, warm air pockets develop between $t$ = 4200 and 5400 s within the RFD cold pool (Figs. 2b–d). By $t$ = 6000 s, nearly the entire RFD cold pool is warmed to the base-state temperature (Fig. 2e). The origin of these warm air surges is from the inflow immediately ahead of the RFGF, as inferred from near-zero $\theta_e'$ (Figs. 3c–g) and verified through backward parcel trajectories (not shown). The descent of inflow air behind the RFGF is similar to the process observed by Riganti and Houston (2017) in the rear flank outflow of a supercell. At $t$ = 7200 s,

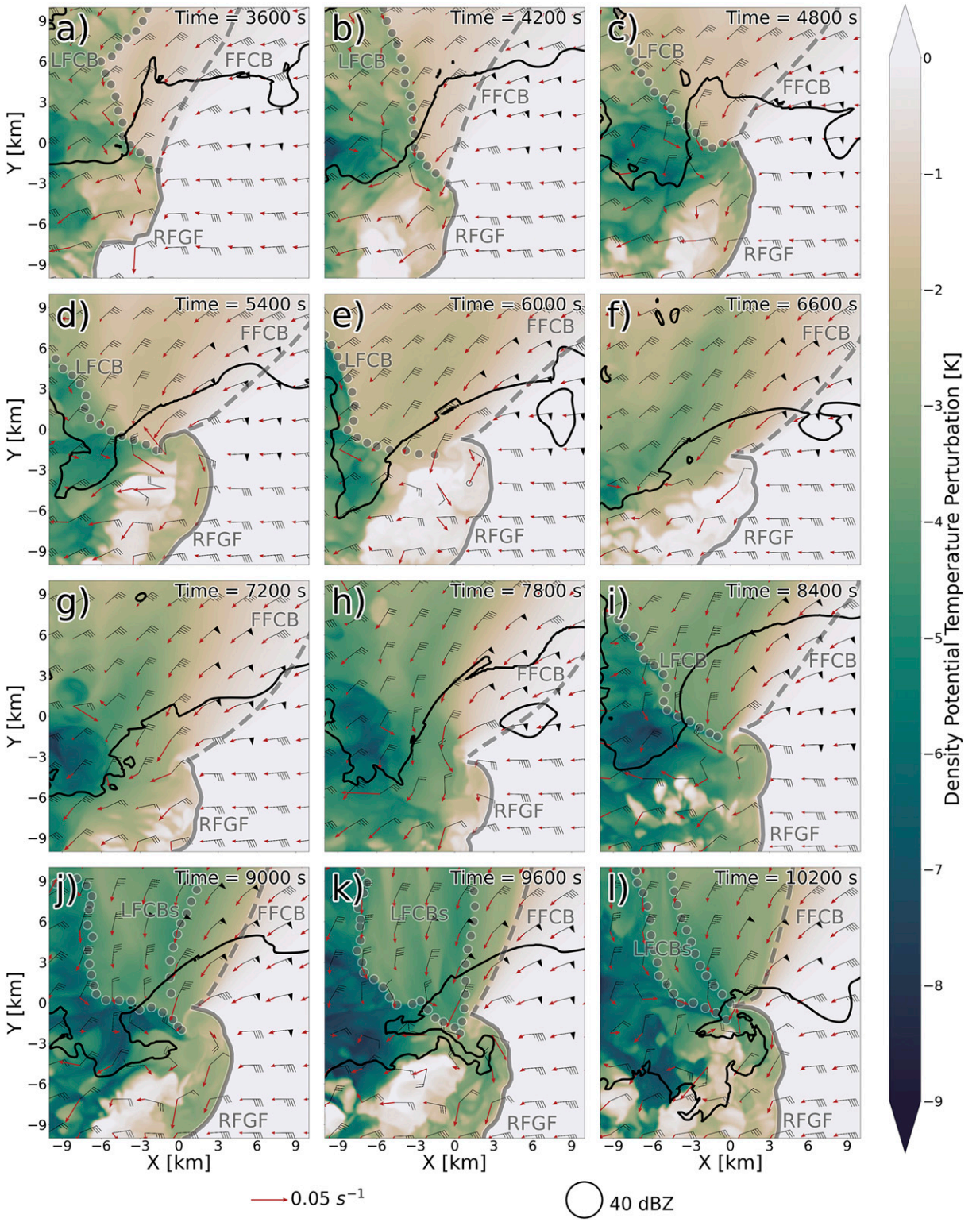


FIG. 2. Plan views of lowest-model-level (12.5 m AGL) $\theta'_\rho$ (K, green shaded), 0–1 km AGL mean horizontal vorticity ($s^{-1}$, red vectors), 0–1 km AGL mean storm-relative winds (kt, black barbs), simulated reflectivity contoured at 40 dB$Z$ (black contours), and relevant surface boundaries subjectively identified every 600 s from (a) 3600 to (l) 10 200 s.

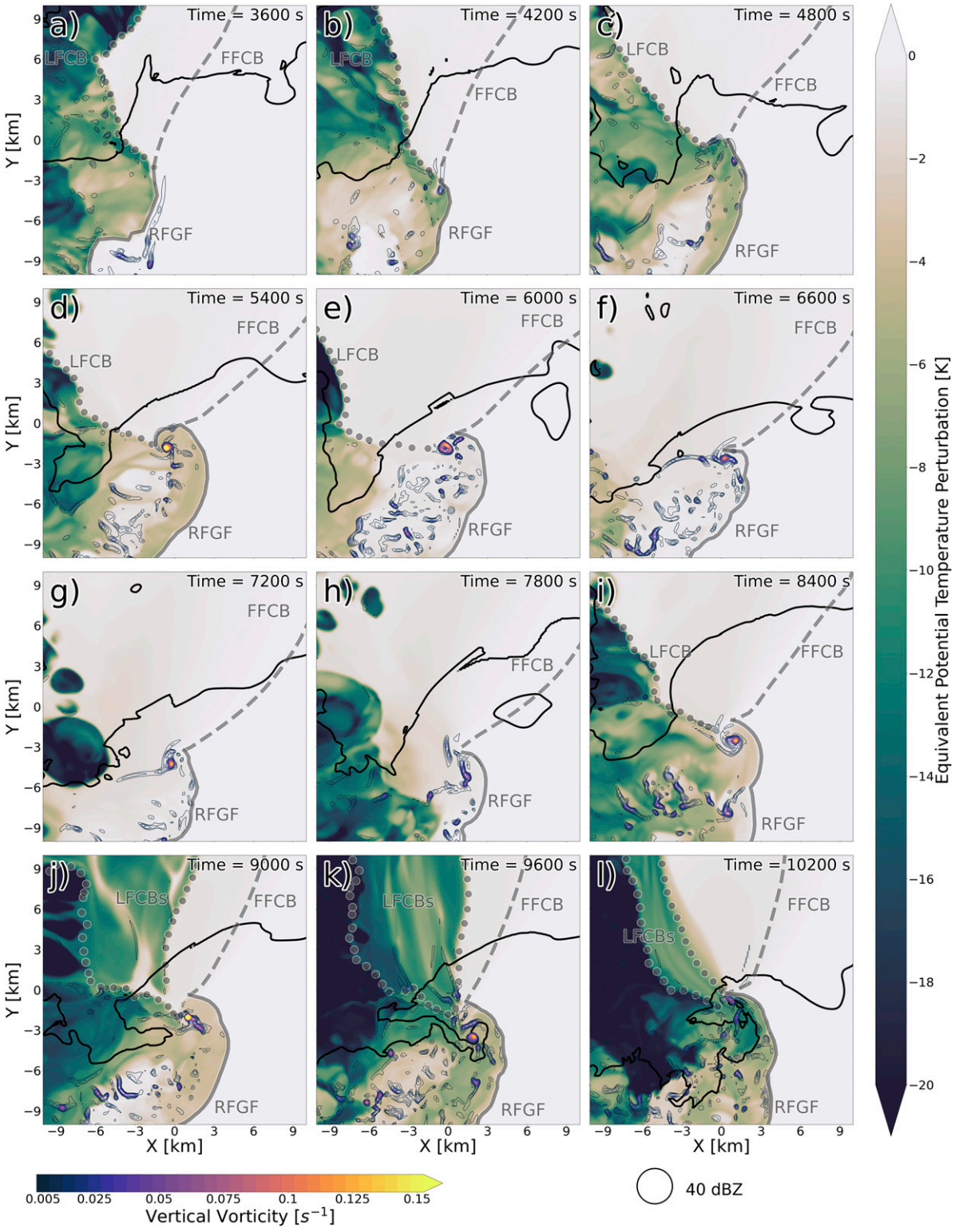


FIG. 3. Plan views of lowest-model-level (12.5 m AGL) $\theta_e'$ (K, green shaded), lowest-model-level (12.5 m AGL) vertical vorticity (s$^{-1}$, blue to yellow contours), simulated reflectivity contoured at 40 dB$Z$ (black contours), and relevant surface boundaries subjectively identified every 600 s (a) from 3600 to (l) 10 200 s.

evaporative cooling from precipitation within the RFD begins to redefine the RFGF with $\theta'_\rho \sim -3$ K (Fig. 2g). Shortly after, downdraft air, possibly in the form of an RFD internal surge (Lee et al. 2012; Skinner et al. 2014; Riganti and Houston 2017), is present behind the RFGF at $t = 7800$ s. The RFGF remains reinforced by cool RFD air characterized by $\theta'_\rho \sim -3$ K and $\theta'_e \sim -8$ K until the end of the analysis period (Figs. 2i–l and 3i–l).

The FFCB thermodynamic gradient is weak and diffuse at the start of the analysis period ($t = 3600$–$6000$ s, Figs. 2a–e). From $t = 6000$–$7800$ s, continuous precipitation in the forward flank, east of the LFCB, evaporatively cools the inflow air. This inflow modification creates a $\theta_\rho$ anomaly of $\sim -4$ K (Figs. 2e–h), compared to $\sim -1.5$ K found at the start of the period. The $\theta_\rho$ gradient sharpens from $t = 8400$ to 10 200 s as the evaporation of forward-flank precipitation further invigorates the eastern extent of the forward-flank cold pool (Figs. 2i–l), and convergence increases. Between $t = 7800$ s and $t = 10\,200$ s, the FFCB begins rotating counterclockwise around the triple point, becoming more north–south-oriented by the end of the time period (Figs. 2h–l). Prior to $t = 7800$ s, the orientation of the FFCB is roughly constant to the northeast, with the 0–1 km AGL mean flow and mean horizontal vorticity vectors remaining roughly parallel to the boundary within this region.

Appreciable positive vertical vorticity ($>0.005\ \mathrm{s}^{-1}$) at the lowest model level (12.5 m AGL) is primarily situated along the LFCB and within the rear-flank cold pool throughout the simulation. The vertical vorticity spatial distribution only changes toward the end of the analysis period from $t = 9000$ to 10 200 s (Figs. 3j–l), where multiple filaments of vertical vorticity are positioned along thermodynamic boundaries. At $t = 4800$ s, vertical vorticity accumulates near the triple point (Fig. 3c) and creates a strong tornado-like vortex (TLV)[2] right before $t = 5400$ s with a peak vertical vorticity of $0.238\ \mathrm{s}^{-1}$ (Fig. 3d). The TLV formation is nearly concurrent to the aforementioned warm pockets in the RFD reaching the triple point. At $t = 8400$ s, as the aforementioned RFD internal surge reaches the triple point, another strong TLV forms with a peak vertical vorticity of $0.19\ \mathrm{s}^{-1}$ (Fig. 3i).

To better understand where the SVC is situated relative to the aforementioned features, the 0–1 km AGL vertically integrated streamwise vorticity (proportional to storm-relative helicity) is used. Initially weak at $t = 3600$ s, the amount of streamwise vorticity within the lowest kilometer begins to increase with time, first in the vicinity of the triple point, and then along and behind the FFCB (Fig. 4a). The local maximum of streamwise vorticity near the triple point is where the SVC is tilted into the vertical underneath the updraft. Periodically, strong pockets of streamwise vorticity are present along the LFCB, particularly in the vicinity of the triple point (Figs. 4d,i,j,k,l), where favorable wind direction and ample horizontal stretching is collocated with a strong thermodynamic boundary. The inflow low (Davies-Jones 2002) as seen in the pressure perturbation field, is situated northeast of the triple point and covers a broad area initially ($t = 3600$–$6000$ s, Figs. 4a–e). There is also a trough branching off the inflow low, situated along the axis of the SVC. Additional transient regions of negative pressure perturbation are collocated with strong realizations of the streamwise vorticity along the LFCB (Figs. 4d,i). At $t = 6600$ s and beyond, the inflow low diminishes in size, and combines with the SVC pressure perturbation (Figs. 4f–l). This coupling enables strong horizontal stretching along the axis of the SVC.

### b. Vertical cross-sectional structure

To further elucidate the structure of the FFCB, simulated RHIs are created to assess the horizontal continuity of the SVC at $t = 9600$ s (Fig. 5), and temporal continuity (Fig. 6). A ubiquitous feature in almost all of these RHIs is a breaking wave in the head of the density current. This feature is visible as a C-shaped structure in the $\theta'_\rho$ field between 5 and 6 km range and below 1 km AGL, where dense air is being lifted and wrapped around a vortex (Figs. 5b,g,l,q and 6l,q). As will be expanded upon later, the structure and evolution of this feature are consistent with those of a Kelvin–Helmholtz (KH) billow and associated vortex, and it will be referred to as such going forward. Near the updraft (azimuth = 280°, Fig. 5a), the depth of the KH billow is much larger than farther away from the updraft (azimuth = 310°, Fig. 5p) where the feature weakens toward the very low levels but does not completely disappear. The radial velocity field shows inbound velocities coincident with the low-$\theta'_\rho$ air as the outflow pushes toward the radar location. A local maximum in outbound velocity is positioned directly above the strong inbound velocity across all azimuths immediately behind the FFCB head. This shearing zone, generally coincident with the KH billow identified in the $\theta'_\rho$ field, is the KH vortex located in the center of the KH billow. The SVC is apparent in an analysis of the inferred vorticity (Figs. 5e,j,o,t), where positive vorticity in the RHI is oriented toward the updraft and is maximized on the periphery of the KH billow and trailing cold pool. Throughout all the azimuths, a negative pressure perturbation is coincident, and dynamically consistent with a nonlinear dynamic pressure perturbation from the KH vortex.

The presentation of the KH billow and enhanced vorticity are characteristic of the mature SVC at $t = 9600$ s. Earlier in the simulation, between $t = 4200$ and 6000 s, an initial SVC forms on the FFCB (not shown). It is characterized by enhanced vorticity and a small KH billow, but the cold pool $\theta'_\rho$ is small ($-1$ K) and the FFCB density gradient weakens considerably by $t = 7800$ s. By $t = 8400$ s, the FFCB density gradient again strengthens and a local maximum in vorticity is coincident with the FFCB head and collocated with a negative pressure perturbation lobe (Figs. 6g,h,j). At $t = 9000$ s, a subtle KH billow, as seen in $\theta'_\rho$, forms on the FFCB and the vorticity, along with the attendant pressure perturbation, strengthens (Figs. 6l,m,o). At $t = 10\,200$ s, three areas of local maxima in vorticity are located on the nose of the FFCB, in the center of the KH billow, and above the trailing cold pool (Fig. 6t).

[2] A TLV is defined when a vertically contiguous region of $\zeta \geq 0.05\ \mathrm{s}^{-1}$ contains 20 or more vertical grid points (500 m) in the lowest 1 km with $\zeta \geq 0.15\ \mathrm{s}^{-1}$ for over 5 continuous minutes.

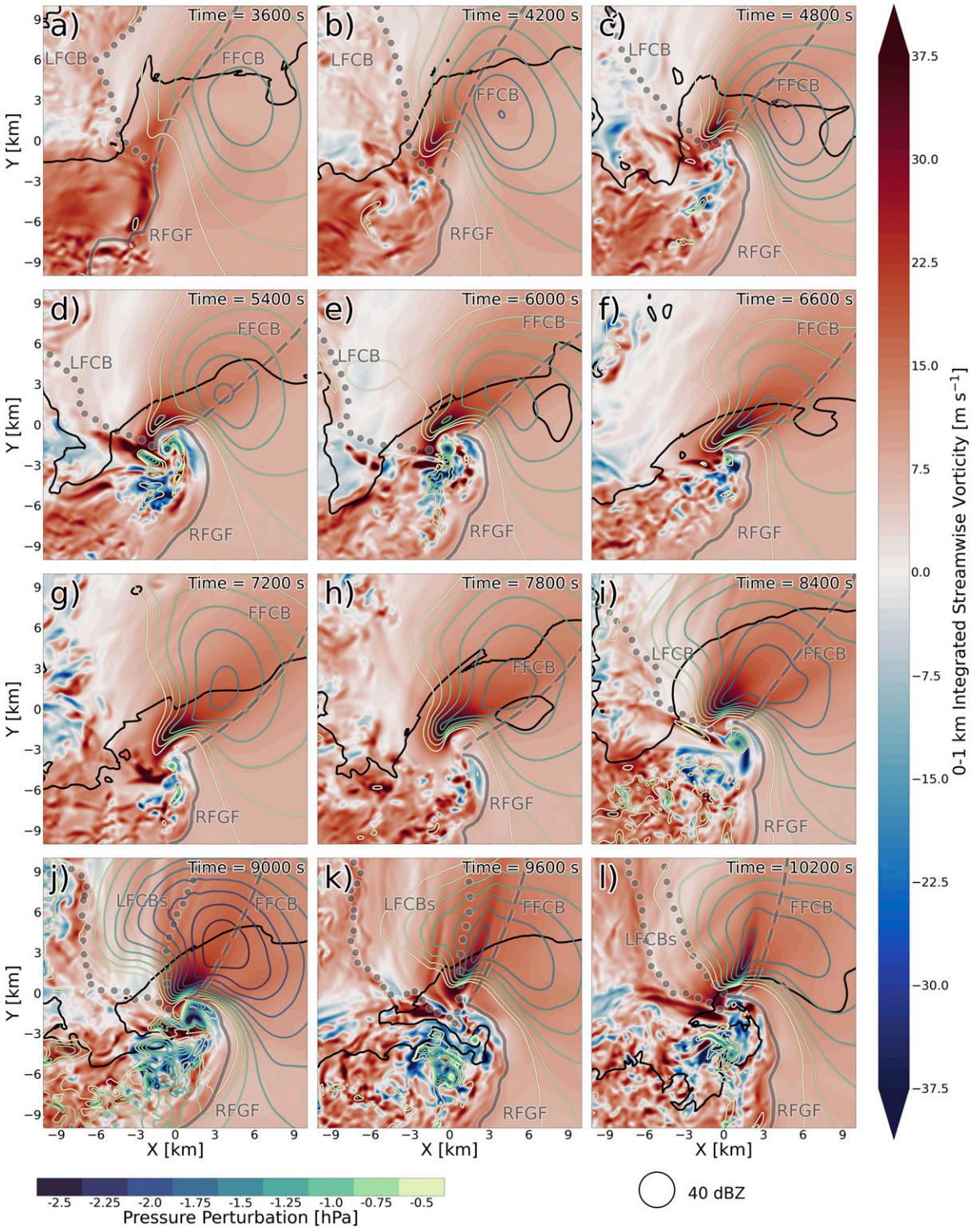


FIG. 4. Plan views of 0–1 km AGL vertically integrated streamwise vorticity (m s$^{-1}$, blue to red shaded), lowest-model-level (12.5 m AGL) pressure perturbation (hPa, blue to green contours, positives not plotted), simulated reflectivity contoured at 40 dB$Z$ (black contour), and relevant surface boundaries subjectively identified every 600 s from (a) 3600 to (l) 10 200 s.

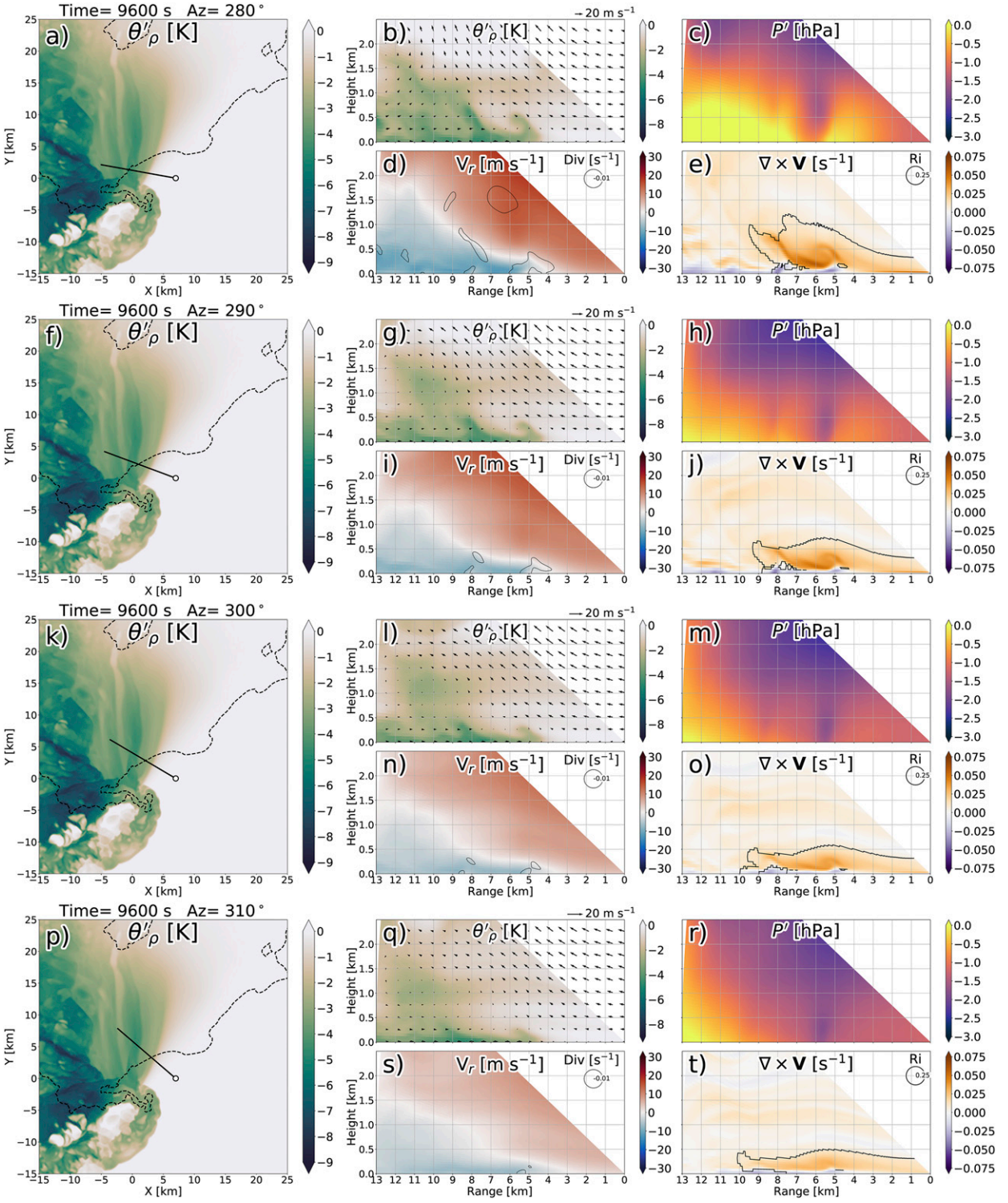


FIG. 5. Lowest-model-level (12.5 m AGL) plan views of $\theta'_\rho$ (K, green shaded) and simulated reflectivity contoured at 40 dB$Z$ (black dashed contours) at $t = 9600$ s with simulated RHI azimuths (a) 280°, (f) 290°, (k) 300°, and (p) 310° along the black line relative to the radar location (white dot). Simulated RHI scans of (b),(g),(l),(q) $\theta'_\rho$ (K) and plane-parallel wind vectors (m s$^{-1}$); (c),(h),(m),(r) pressure perturbation (hPa); (d),(i),(n),(s) radial velocity (m s$^{-1}$) and divergence (contoured at $-0.01$ s$^{-1}$); and (e),(j),(o),(t) horizontal perpendicular vorticity (s$^{-1}$) and Richardson number (contoured at 0.25) for each RHI azimuth.

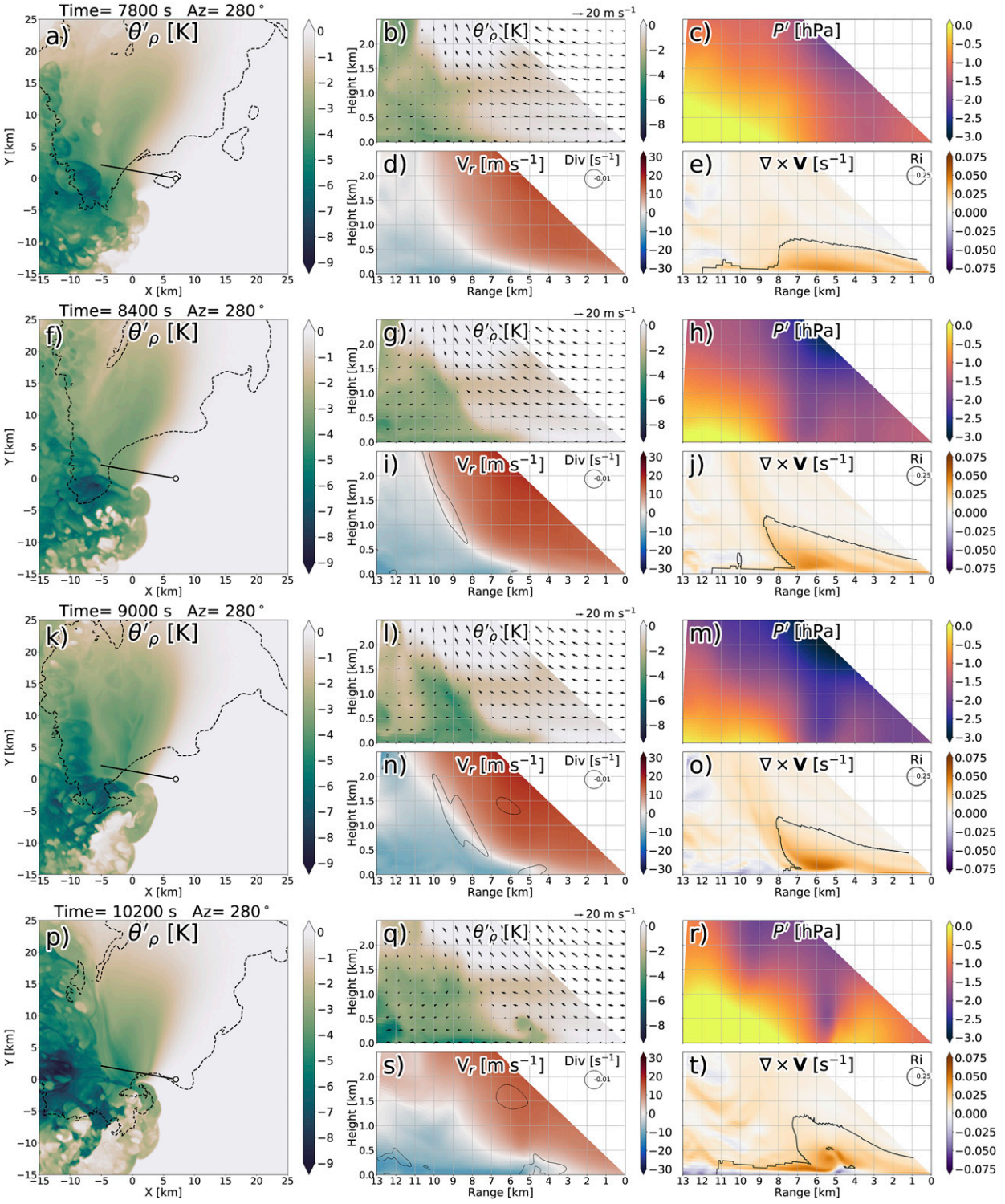


FIG. 6. Lowest-model-level (12.5 m AGL) plan views of $\theta'_\rho$ (K, green shaded) and simulated reflectivity contoured at 40 dB$Z$ (black dashed contour) for $t$ = (a) 7800, (f) 8400, (k) 9000, and (p) 10 200 s. Simulated RHI azimuth 280° is along the black line relative to the radar location (white dot). Simulated RHI scans of (b),(g),(l),(q) $\theta'_\rho$ (K) and plane-parallel wind vectors (m s$^{-1}$); (c),(h),(m),(r) pressure perturbation (hPa); (d),(i),(n),(s) radial velocity (m s$^{-1}$) and divergence (contoured at $-0.01$ s$^{-1}$); and (e),(j),(o),(t) horizontal perpendicular vorticity (s$^{-1}$) and Richardson number (contoured at 0.25) for each output time.

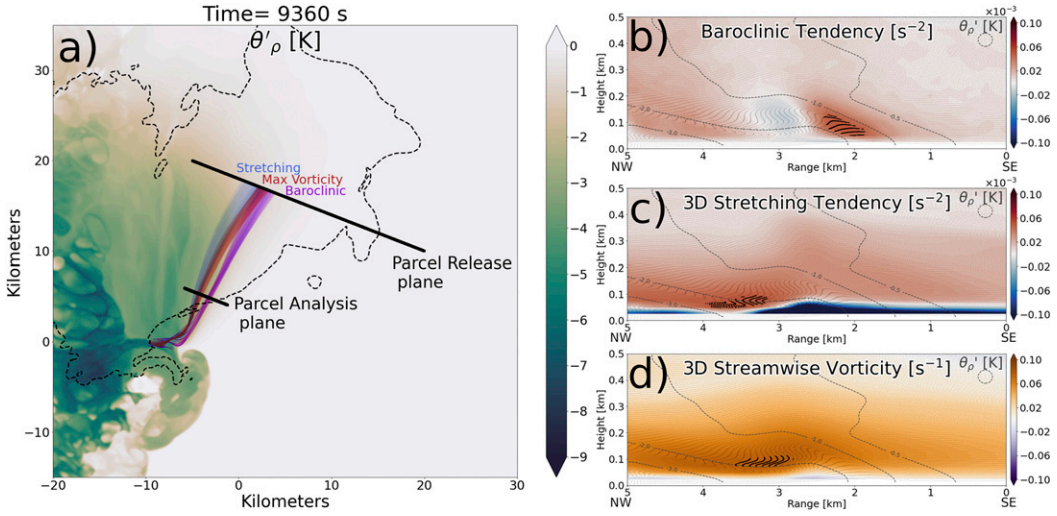


FIG. 7. (a) Lowest-model-level (12.5 m AGL) plan views of $\theta'_\rho$ (K, green shaded) and simulated reflectivity contoured at 40 dB$Z$ (black dashed contour) at $t = 9360$ s, the mean time at which parcels transect the analysis plane. The vertical plane where all parcels are released is annotated, as well as the parcel analysis plane. The 312 parcels in the baroclinic regime, stretching regime, and max vorticity region are color coded purple, blue, and red, respectively. (b) The parcel baroclinic tendency (s$^{-2}$, red to blue shaded) is gridded to the analysis plane. All parcels are shown in light gray dots, parcels within the baroclinic regime are denoted by black bold dots. $\theta'_\rho$ is contoured at −0.5, −1, −2, and −3 K. (c) As in (b), but with 3D stretching tendency (s$^{-2}$, red to blue shaded) and parcels within the stretching regime are denoted by black bold dots. (d) As in (b), but with streamwise vorticity magnitude (s$^{-1}$, orange to purple shaded) and parcels within the max vorticity region are denoted by black bold dots.

## 4. Parcel analysis

Between $t = 9000$ and 9600 s, the SVC is well defined compared to other times in the simulation, with strong streamwise vorticity present over a long stretch of the FFCB (Figs. 4i,k). Therefore, at $t = 8640$ s, 200 000 parcels are released approximately 20 km upstream of the updraft, such that they reach the updraft at approximately $t = 9540$ s. The parcels are released in a vertically oriented plane along a horizontal line from ($x$, $y$) = (−5, 20) km to (20,10) km; and extending from the surface to 1 km AGL (Fig. 7a). This plane is on the northeastern edge of the forward-flank cold pool directly upstream of the FFCB and SVC.

The parcels within the SVC achieve a maximum in 3D vorticity magnitude at approximately $t = 9360$ s. To investigate the magnitude and spatial distribution of the pertinent forcings to the SVC, an analysis plane is generated, parallel to the initial release plane, and nearly orthogonal to the FFCB. The parcel data at the point each parcel crosses the analysis plane is cubic spline interpolated to a grid on that plane, implementing the same spacing as the parent CM1 configuration (125-m horizontal grid spacing, 25-m vertical grid spacing). Due to deformation in the flow upstream, parcels transect the plane at slightly different times. The time at which each parcel is closest to the plane is used for analysis, resulting in an average parcel-intersection time of approximately $t = 9360$ s. The parcels in the extremes of baroclinic tendency, 3D stretching tendency, and streamwise vorticity magnitude are found in the analysis plane to show where each forcing dominates. Of the 32 013 parcels that are present in the analysis plane (compared to the 200 000 parcels total), 312 parcels greater than the 99th percentile of baroclinic tendency ($4.617 \times 10^{-5}$ s$^{-2}$), 3D stretching tendency ($4.887 \times 10^{-5}$ s$^{-2}$), and streamwise vorticity magnitude (0.075 s$^{-1}$) are found for each "regime." The 3D vorticity tendencies (1) of all of these parcels are integrated in time to identify the different forcings contributing to the vorticity in that region. The integrated tendencies are summed together and compared to the interpolated vorticity from the model and match up very well,[3] confirming the accuracy of the individual tendencies.

A dipole in baroclinic tendency is apparent across the FFCB head (Fig. 7b), where positive baroclinic tendency (oriented out of the plane, toward the updraft) is present on the leading

[3] The root-mean-square error (RMSE) and root-mean-square percentage error (RMSPE) of the integrated vorticity budgets compared to the interpolated vorticity were calculated across the 312 parcel trajectories in each region. The mean of the RMSE (RMSPE) of all the parcels in the baroclinic regime, stretching regime, and streamwise vorticity region was 0.0029 s$^{-1}$ (6.70%), 0.0020 s$^{-1}$ (4.95%), and 0.0030 s$^{-1}$ (4.38%), respectively. However, this error is primarily driven by uncertainty in the budgets once the parcels were entrained in the updraft. The mean RMSE (RMSPE) reduces to 0.0014 s$^{-1}$ (3.08%), 0.0010 s$^{-1}$ (1.88%), and 0.0005 s$^{-1}$ (0.85%) for the baroclinic regime, stretching regime, and streamwise vorticity region, respectively, if the parcel trajectory was terminated once it reached 1 km AGL.

edge of the FFCB, and negative baroclinic tendency (oriented into the plane, away from the updraft) is present in the wake of the FFCB head. The parcels in the baroclinic regime (Fig. 7a) stay on the leading edge of the FFCB along their entire trajectory before being tilted up into the updraft, supporting continuous baroclinic production. Continuous baroclinic production is confirmed in Fig. 8a, where temporally integrated baroclinic tendency, averaged over the parcels in the baroclinic regime, steadily increases throughout the entire trajectory. The mean integrated baroclinic tendency and mean integrated stretching tendency of the parcels within the baroclinic regime are of similar magnitude throughout the parcels' trajectories, and both contribute $\sim 0.02\,s^{-1}$ of vorticity by the analysis time ($t = 9360$ s). After the plane transect, these parcels continue to acquire more vorticity baroclinically before being lifted into the updraft.

Strong negative values in stretching tendency exist near the surface in the vicinity of the FFCB (Fig. 7c) due to the streamwise stretching of antistreamwise vorticity, whereas positive values are broadly stratified between 100 and 300 m AGL where the inflow low and streamwise vorticity are collocated. The maximum, however, lies in the wake of the FFCB head due to the KH vortex pressure perturbation, which leads to horizontal acceleration of the flow. The parcels within this stretching regime originate farther northwest than the parcels in the baroclinic regime (Fig. 7a), and have a more curved trajectory, arcing toward the SVC axis as they approach the updraft. In the stretching regime, the mean integrated stretching tendency dominates the overall vorticity evolution, contributing on average over $0.04\,s^{-1}$ in the 720-s integrated trajectory (Fig. 8b). The mean integrated baroclinic tendency, however, is much weaker, generating on average $<0.01\,s^{-1}$ along the trajectory by the analysis period. The total magnitude of vorticity is much larger in this regime compared to the baroclinic regime due to the large increase in stretching despite a smaller contribution of baroclinic generation. After the analysis time, along-stream convergence and deceleration causes the vorticity magnitude to decrease as the parcels approach the base of the updraft. Despite the negative vorticity tendency, the accrued vorticity along the parcels' trajectories is not fully cancelled out, and thus remains much larger than the base-state 3D vorticity magnitude of $0.02\,s^{-1}$.

As seen in Figs. 5 and 6, streamwise vorticity is generally maximized in the vicinity of the KH vortex, while large values also exist on the nose of the FFCB (baroclinic regime) and on top of the trailing cold pool (stretching regime, Fig. 7d). The parcels that reside in the maximum vorticity region in the analysis plane originate in between the baroclinic regime parcels and the stretching regime parcels (Fig. 7a). Along their trajectory, they generally follow the southern side of the stretching parcel grouping until the analysis plane, at which point the two groupings are nearly collocated. Indeed, a number of the parcels within the maximum vorticity region are the same parcels identified in the stretching regime (Figs. 7c,d). This overlap is further illustrated in the vorticity budgets, where the vorticity budgets of the parcels in the maximum vorticity region share similar evolutions as those in the stretching regime (Figs. 8b,c). The maximum 3D vorticity is nearly $0.08\,s^{-1}$, approximately 4 times larger than the base-state 3D vorticity magnitude of $0.02\,s^{-1}$ (Fig. 8c). Note that, comparing Figs. 7b and 7d, the parcels in the maximum vorticity region are also located in the negative baroclinic part of the dipole, implying that baroclinic tendency is not a primary vorticity contributor when the parcels are within the KH vortex.

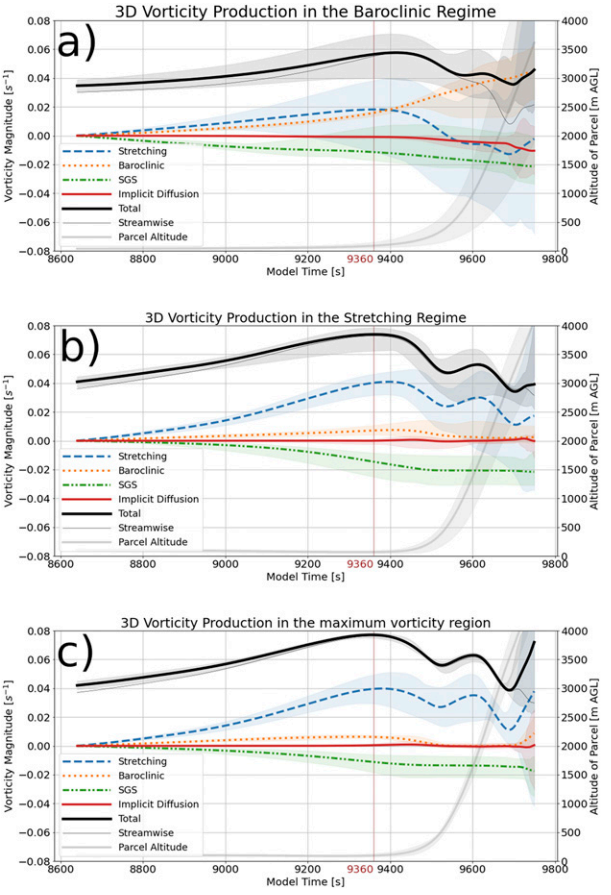


FIG. 8. (a) Time series of the total 3D vorticity budget of the parcels within the baroclinic regime. The mean temporally integrated vorticity components are stretching (blue dashed line), baroclinic (orange dotted line), SGS mixing (green double-dotted–dashed line), and implicit numerical diffusion (red solid line). Coriolis accelerations and explicit diffusion are not included in this simulation. Thick black line is the mean integrated vorticity magnitude, and the thin black line is the mean streamwise component of the vorticity magnitude. The light gray line is the time series of the mean parcel altitude for reference. The shaded intervals show the maximum and minimum of all of the aforementioned time series. (b) As in (a), but for the 312 parcels within the stretching regime. (c) As in (a), but for the 312 parcels within the maximum vorticity region.

## 5. Observations

### a. 8 June 2018

On 8 June 2018, both TTUKa radars deployed on a nontornadic high-precipitation supercell near Norris, South Dakota. No organized low-level mesocyclone was evident

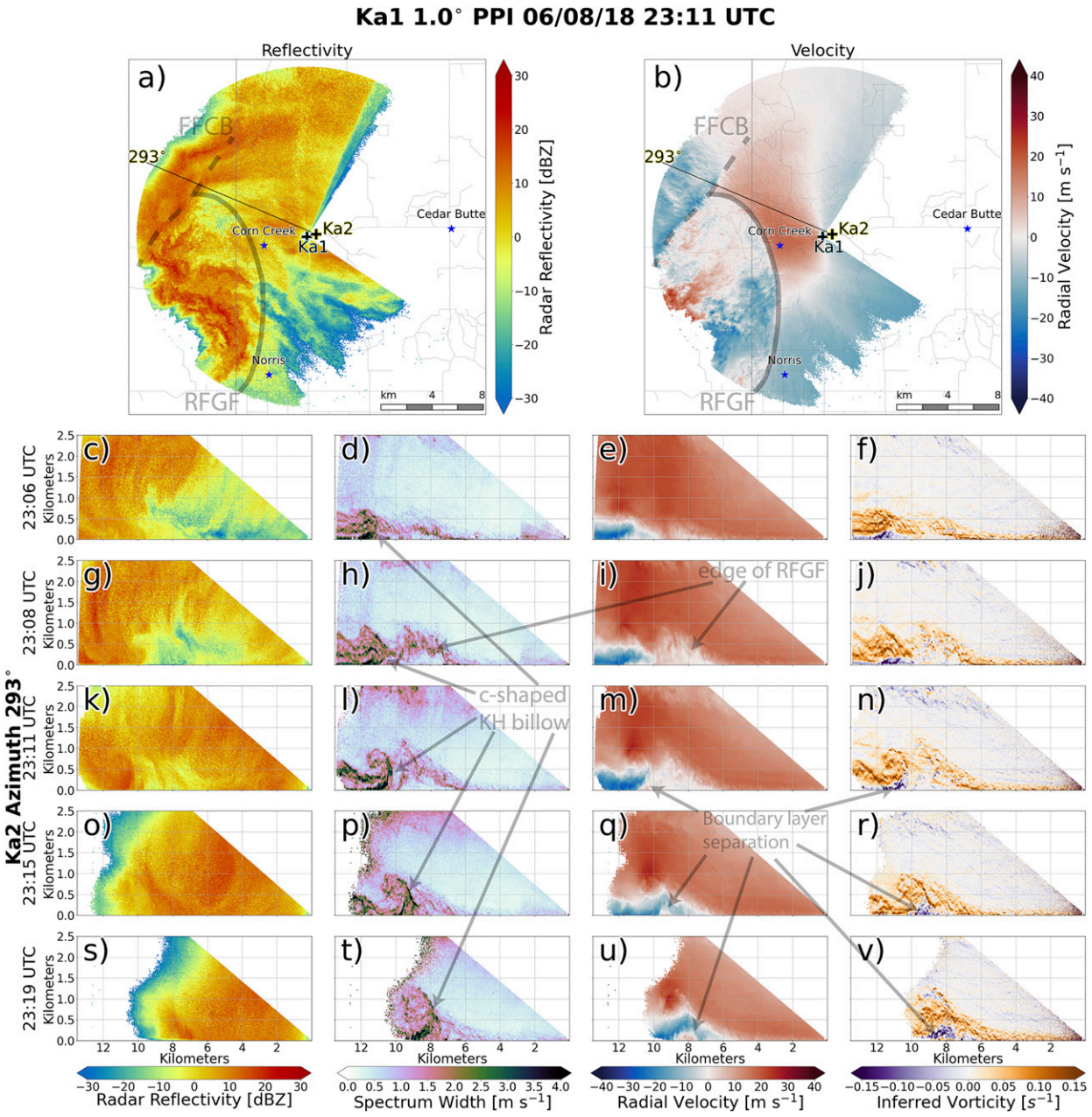


FIG. 9. A PPI scan of (a) reflectivity (dB$Z$, shaded) and (b) radial velocity (m s$^{-1}$, shaded) from TTUKa1 gathered at 2311 UTC 8 Jun 2018 at 1° elevation. The RFGF and FFCB are annotated. (c)–(v) A series of five RHIs (rows) over a duration of 780 s from TTUKa2 at a constant azimuth 293°. The columns in (c)–(v) are (left to right) reflectivity (dB$Z$, shaded), spectrum width (m s$^{-1}$, shaded), radial velocity (m s$^{-1}$, shaded), and inferred vorticity (s$^{-1}$, shaded).

visually or on PPIs during this deployment. On the PPIs gathered by TTUKa1 (Figs. 9a,b), the RFGF delineates a broad, turbulent area of inbound velocities west of the radars from the relatively laminar inflow velocities to the east. There was precipitation throughout the inflow region ahead of the storm, with no clear delineation between the forward-flank precipitation and the numerous feeder cells, all being relatively nondescript in terms of velocity. There was, however, an identifiable kinematic boundary intersecting the RFGF west-northwest of the radars at around 6-km range. This boundary, assumed to be the FFCB, extended northeast away from the RFGF and into the forward-flank precipitation until it was out of range of the TTUKa radars.

TTUKa2 gathered a swath of RHIs spaced 10° in azimuth apart, ranging from 193° to 3° north-relative azimuth (Figs. 9c–v). This analysis focuses on azimuth 293°, where the FFCB can

be fully resolved in all times with respect to range, attenuation, and structure. Azimuth 283° also shows the FFCB head, but the FFCB head is partially lost due to range and attenuation. Azimuths larger than 293° also show a compact FFCB head; however, the depth is shallower and the shearing zone is weaker.

Spectrum width is primarily used to find regions of turbulent motion, and, in this case, reveals a detailed FFCB vertical structure (Figs. 9d,h,l,p,t). A strong C-shaped region of spectrum width, indicative of the head of the FFCB, exists in the lowest kilometer AGL at a range of 11 km at the beginning of the analysis period, moving to a range of 8 km by the end of the analysis period. The C-shaped region is in line with the KH billow identified in the simulated RHIs, and is identifiable as such due to the turbulence within and on the periphery of the density current head.

In the first two RHIs at 2306 and 2308 UTC, there is a small area of weak radial velocities $\sim 0\,\mathrm{m\,s^{-1}}$ and weak spectrum width values $< 2.5\,\mathrm{m\,s^{-1}}$, near the surface, and at approximately 8-km range, where the radar samples the northern bowing edge of the RFGF ahead of the FFCB. The FFCB is easily identified by stronger inbound radial velocities $< -10\,\mathrm{m\,s^{-1}}$ and spectrum width values $> 3\,\mathrm{m\,s^{-1}}$ beyond 10-km range (Figs. 9d,e,h,i).

Strong inbound velocities ($< -20\,\mathrm{m\,s^{-1}}$) are present near the surface beyond 10-km range initially, and follow the progression of the FFCB nose with time (Figs. 9e,i,m,q,u). This maximum inbound velocity exists immediately under a local maximum in the outbound radial velocity at around 1 km AGL. Ahead of this radial velocity couplet, the inbound velocities generally nose up above the surface slightly in response to the KH vortex and the adverse pressure gradient causing boundary layer separation.[4]

Coincident with the radial velocity couplet, a broad area of positive inferred vorticity is present; the vorticity vector is oriented out of the plane (i.e., a northeasterly component), and toward the updraft (Figs. 9f,j,n,r,v). Filaments of positive vorticity are concentrated in the KH vortex, above the trailing cold pool, and on the front nose of the FFCB, all indicative of the enhanced vorticity of the SVC.

### b. 12 June 2018

On 12 June 2018, both TTUKa radars deployed on a nontornadic cluster of storms that became a "classic" supercell in the Oklahoma Panhandle near Gate, Oklahoma. Midlevel winds were generally weak (approximately $12\,\mathrm{m\,s^{-1}}$ at 500 hPa), but a northwest flow regime was in place such that the forward-flank precipitation sagged southeast of the mesocyclone.

When first deploying at 0038 UTC, the RFD precipitation was located northwest of the radars (Figs. 10a,b). At the beginning of the deployment, a robust kinematic boundary existed within the forward-flank precipitation, approximately 7 km north of the radars between azimuths 342° and 82° (identified as the primary FFCB). The boundary was best defined at the beginning of the deployment, but slowly diminished over the following 900 s. Considerable radial convergence existed along the length of this boundary, with nearly $40\,\mathrm{m\,s^{-1}}$ of radial velocity difference across portions of the boundary on the 1° TTUKa1 PPI. Another region of inbound velocities exists at 3 km range, north/northeast of the radars (identified as the leading FFCB). The leading FFCB is likely associated with a weak wind shift and thermal gradient, where the primary FFCB likely has a much stronger wind shift and thermal gradient. However, no in situ observations were available to verify the thermodynamic nature of these boundaries.

TTUKa2 gathered a swath of RHIs spaced 10° in azimuth apart, ranging from 252° to 122° azimuth (Figs. 10c–v). This broad swath of RHIs gathered data on the vertical structure throughout the entire supercell, from south of the RFD into the southern edge of the forward flank. In particular, the 352° to 32° azimuths are focused on because they were oriented most orthogonal to the robust FFCB and near the updraft.

For the 352° and 2° azimuths, the reflectivity shows a pronounced KH billow identified by strong reflectivity, where scatterers were advected around the KH vortex. The KH billow is found between 4 km and roughly 8 km range, and from the surface to 1.5 km AGL (Figs. 10c,g). Using spectrum width, the outflow head is better distinguished by a region of values $> 1\,\mathrm{m\,s^{-1}}$, a stark contrast to the inflow air with spectrum width values near $0\,\mathrm{m\,s^{-1}}$ (Figs. 10d,h,l,p,t). The 352° azimuth has very strong outbound velocities, $> 40\,\mathrm{m\,s^{-1}}$ at the top and above the FFCB head with inbound velocities $\sim 10\,\mathrm{m\,s^{-1}}$ near the surface (Fig. 10e). The magnitude of the vertical shear around the KH vortex slowly decreased farther away from the updraft; however, strong inbounds at the surface remain immediately behind the primary FFCB, especially east of azimuth 32°. In the 2° azimuth, a strong compact horizontal vortex (likely the KH vortex) exists at 7-km range and 0.75 km AGL (Figs. 10i,j). The presence of strong vorticity ($\sim 0.45\,\mathrm{s^{-1}}$) is likely an extreme manifestation of the KH vortex; strong vorticity is also present above the trailing cold pool and, to a lesser extent, the FFCB leading edge, which is all representative of the strong SVC.

## 6. Discussion

In both the 8 June and 12 June observed SVC cases, an identifiable KH billow was found within the head of the FFCB near the updraft, similar to the simulated RHIs. On 8 June, the KH billow was approximately 4 km in length, extending from within the RFD cold pool to 1 km just northeast of the intersection between the RFGF and FFCB. The KH billow was on average 2 km deep within the RFD cold pool (not shown), 1 km deep at the intersection of the RFGF and FFCB (Figs. 9d,h,l,p,t), and 0.5 km deep approximately 1 km

[4] An adverse pressure gradient occurs when the pressure increases nonhydrostatically, consistent with convergence of the inflow and outflow at the boundary interface. The positive pressure gradient immediately behind the nose of the FFCB causes the boundary layer flow to detach from the surface and lift up, inducing a region of negative vorticity in the recirculation (Batchelor 1967).

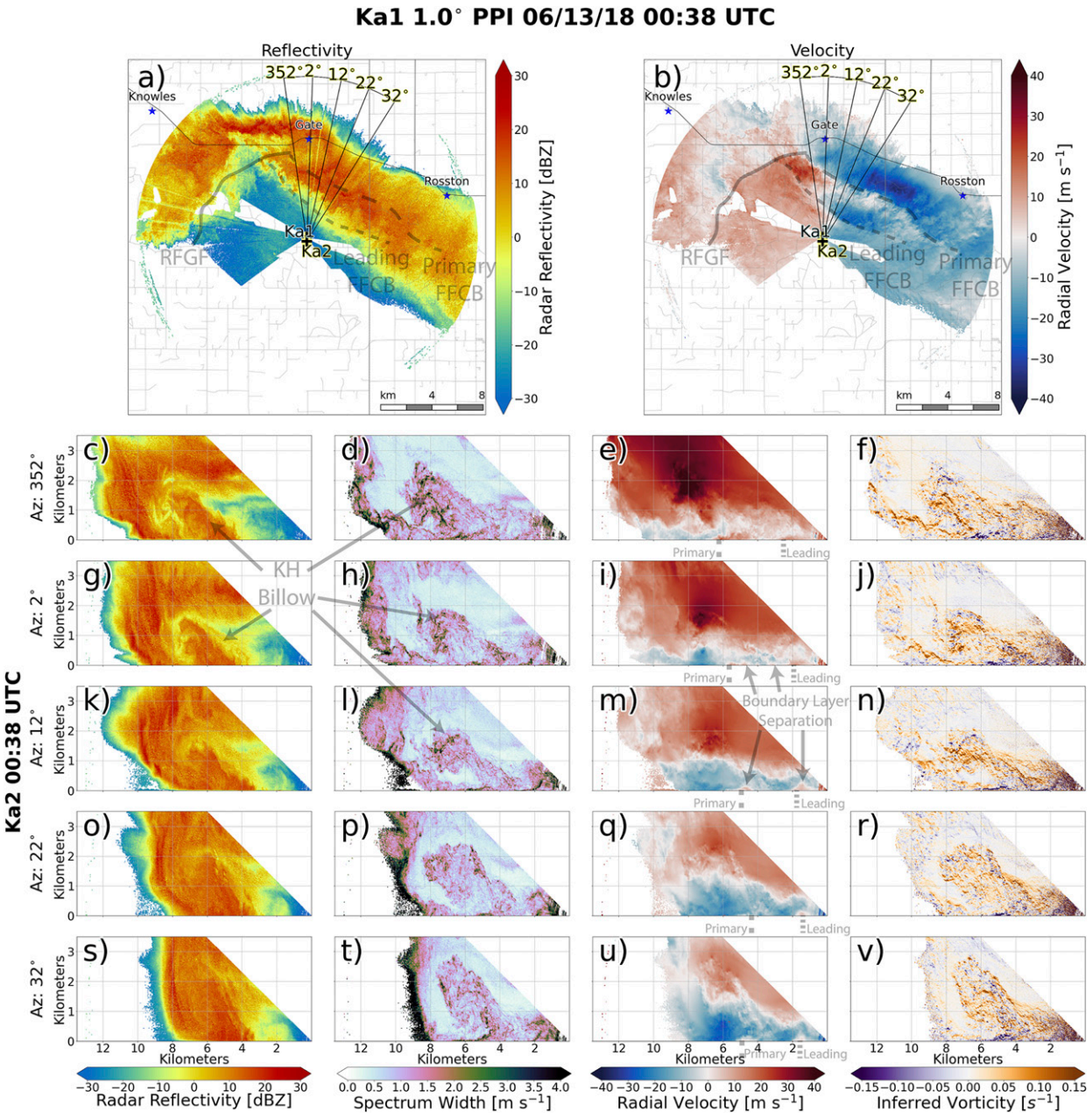


FIG. 10. A PPI scan of (a) reflectivity (dB$Z$, shaded) and (b) radial velocity (m s$^{-1}$, shaded) from TTUKa1 gathered at 0038 UTC 13 Jun 2018 at 1° elevation. The RFGF and FFCBs are annotated. (c)–(v) A series of five RHIs (rows) from TTUKa2 at a constant time with azimuths ranging from 352° to 32°. The columns in (c)–(v) are (left to right) reflectivity (dB$Z$, shaded), spectrum width (m s$^{-1}$, shaded), radial velocity (m s$^{-1}$, shaded), and inferred vorticity (s$^{-1}$, shaded).

northeast of the boundary intersection (not shown). The KH billow found in the 12 June case remained approximately the same size over 9 km along the FFCB (approximately 2 km deep). However, the vorticity within the SVC did decrease farther away from the updraft. The KH billow decreased in depth beyond 10 km away from the updraft (not shown).

The SVC demonstrated temporal consistency for both of the radar cases discussed. On 8 June, the SVC likely existed before the beginning of the first deployment at 2306 UTC and lasted until the end of the deployments at 2338 UTC (not shown). The KH vortex and associated KH billow on 12 June lasted from 0038 to 0044 UTC before dissipating. However, the SVC was likely present before the beginning of the second deployment (that started at 0038 UTC), because there were signs of a KH billow and enhanced vorticity along the FFCB during the brief first deployment at 0025 UTC (not shown).

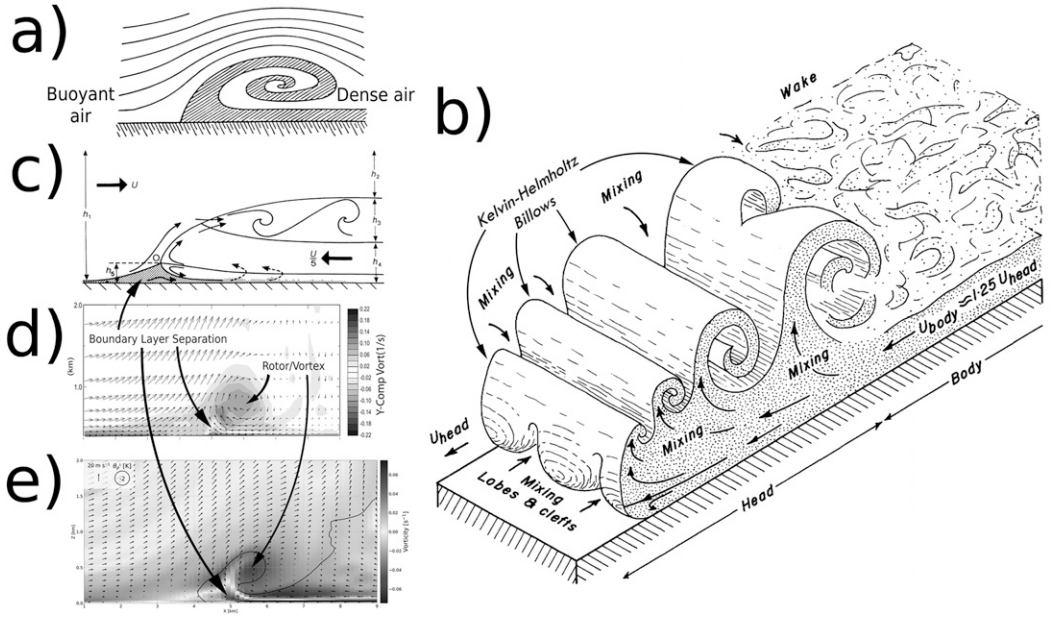


FIG. 11. (a) A conceptual schematic of a singular, large KH billow in the head of a density current from Prandtl (1953). (b) A 3D schematic of a density current, displaying multiple KH billows within the head as well as the size and placement of lobe-cleft instability on the nose from Allen (1985). (c) A 2D vertical cross-section schematic of a density current showing the boundary-relative airflow and the region of boundary layer separation from Simpson and Britter (1980). (d) A model output 2D vertical cross section of vorticity through a rotor that shares a lot of the same qualities as the SVC (Schenkman et al. 2012). (e) The current model output of a 2D vertical cross section through the FFCB and SVC.

The presence of billows within the wake of the head of a density current, is thoroughly established in the literature (Fig. 11) and are the result of Kelvin–Helmholtz instability (KHI). Prandtl (1953) initially proposed the now antiquated conceptual diagram (Fig. 11a), that correctly illustrates the KH vortex in the center of the KH billow, but overstates the degree of roll-up. The conceptual diagram has been further refined in Allen (1985) and Simpson and Britter (1980) (Figs. 11b,c) where instead of a single dominant KH billow, multiple KH billows form on the top of the density current, within and behind the head; and tend to move backward behind the head with time. Schenkman et al. (2012) found a singular horizontal rotor within the head of a density current in a supercell (Fig. 11d), and roughly in the same storm-relative position as the SVC vortex in this study (Fig. 11e). They attribute the origin of the rotor to frictional effects; however, in the present study, the same feature exists without the inclusion of surface friction, further substantiating a separate mechanism. Schenkman et al. (2012) also noted a region of boundary layer separation immediately ahead of the nose of the density current (Fig. 11d) due to an adverse pressure gradient; Simpson and Britter (1980) share these findings as well (Fig. 11c). While both of these authors attributed it to surface friction effects, the simulated RHIs in this study show negative vorticity (oriented away from the updraft) very close to the surface under the nose and head of the density current (Figs. 5b,g,l, 6q, and 11e), despite the bottom boundary condition being free slip. Additionally, there is a weak local maximum in pressure perturbation immediately ahead of the density current nose (Figs. 5c,h,m,r) that could cause enough of an adverse pressure gradient to support boundary layer separation. The observed RHIs also corroborate the existence of this feature. Simpson (1972) states that the buoyant air trapped underneath the dense air can initiate lobe-cleft instability due to the release of gravitational instability, and create counterrotating vertical vortices on either side of the cleft as the buoyant air rises. Numerous finescale velocity signatures of inbound and outbound velocities packed closely together at the FFCB interface (Figs. 9b and 10b) may be indicative of these vortices forming along the FFCB; which is in line with the ''parade of vortices'' observed in ORF17.

Early in the supercell evolution, the rain cooled inflow air may only be slightly modified, enough to create a shallow, weak deformation/baroclinic zone (e.g., Fig. 6b). The confluence along this interface will tighten the thermodynamic boundary (Cohen and Schultz 2005; Betten et al. 2018) and create a focus for environmental vorticity accumulation in addition to baroclinic vorticity generation, resulting in a relatively horizontal vortex sheet. The Richardson number in this region remains below the critical value of 0.25 (Figs. 6d,i,n,s,x), supporting the development of KHI. A perturbation of adequate wavelength to this vortex sheet will amplify, causing the vortex sheet to roll up (Miles and Howard 1964; Batchelor 1967, their Fig. 7.1.3). Due to the density stratification across the vortex sheet, once KHI is released, baroclinic vorticity production is active on the

sloped isentropes (Fig. 7b). Positive (oriented toward the updraft) baroclinic tendency is present at the leading edge of the FFCB, whereas negative (oriented away from the updraft) baroclinic tendency is collocated with the developing KH vortex (comprised of positive vorticity). Furthermore, these processes are occurring in a region with strong boundary-parallel acceleration toward the updraft, due to the inflow low that acts to stretch the predominantly streamwise vorticity. Therefore, environmental vorticity accumulation along the FFCB head and into the KH vortex is continuously stretched over a pathlength of ~15 km. The amplification of this vorticity by stretching creates a nonlinear dynamic pressure perturbation superposed on the existing inflow low, further accelerating the flow, specifically in the vicinity of the KH vortex. Streamwise vorticity is maximized in the KH vortex at the center of the KH billow, with values in this simulation of $\sim 0.08\,s^{-1}$ driven almost solely by stretching (maximum vorticity region, Fig. 8c). Stretching also dominates the vorticity budgets of parcels on the top surface of the trailing cold pool behind the FFCB (stretching regime), with $\sim 0.07\,s^{-1}$ of streamwise vorticity (Fig. 8b). On the leading edge of the FFCB head, the parcels are within the baroclinic regime, and the vorticity budgets show an approximately equal contribution from stretching and baroclinic generation, totaling $\sim 0.06\,s^{-1}$ of streamwise vorticity (Fig. 8a). The vorticity in all three of these regions are of similar magnitude and ~3–4 times the base-state streamwise vorticity ($\sim 0.018\,s^{-1}$), thus all three regions are considered to constitute the SVC. Numerous studies (Klemp and Rotunno 1983; Brandes 1984; Hane and Ray 1985; Rotunno and Klemp 1985; Wicker and Wilhelmson 1995; Adlerman et al. 1999; Shabbott and Markowski 2006; Markowski et al. 2012; Kosiba et al. 2013; Beck and Weiss 2013; Weiss et al. 2015; Marquis et al. 2016; Orf et al. 2017) have identified the importance of baroclinic vorticity generation in the FFRG region of a supercell as a significant source of vorticity that may end up tilted into the low-level mesocyclone. This study corroborates that theory, in which some of the parcels within the SVC (baroclinic regime parcels) enter the low-level updraft with significant baroclinically generated vorticity. However, the stretching of horizontal streamwise vorticity is the primary mechanism for the strong streamwise vorticity within the SVC, which subsequently enters the low-level mesocyclone.

The boundary-parallel acceleration in this study is the unique driver that, as far as the authors are aware, has not been investigated in previous studies. Parallel flow to a density current has been looked at previously (Weckwerth and Wakimoto 1992; Lee and Wilhelmson 1997; Buban et al. 2012; Krull 2019), resulting in a number of dynamic processes (boundary-perpendicular KH billows, horizontal shearing instability, vertical vortex sheets, and variance in the depth and magnitude of KH billows, respectively). Krull (2019) specifically found that increasing the boundary-parallel component of the shear increases the strength of the vortex in the center of the KH billow, while keeping the vortex lines parallel to the boundary. However, the only study that briefly mentioned the horizontal stretching of flow parallel to the boundary was Schenkman et al. (2012), who attributed the horizontal streamwise stretching as the reason they had a single vortex.

Throughout this paper, the forward-flank boundary has been identified as the FFCB, in line with Beck and Weiss (2013). This is based on its storm-relative position and the fact that the air behind the boundary shows no history of descent, as indicated by negative $\theta'_\rho$ (Fig. 2) and near-zero $\theta'_e$ (Fig. 3). The boundary is initially weakly convergent in this simulation with a broad, diffuse, horizontal (presumably, hydrostatic) pressure gradient, but the convergence and horizontal pressure gradient increase with both time and proximity to the updraft (Figs. 5 and 6d,i,n,s), concurrent with the strengthening SVC. Later, other features, characteristic of a density current are apparent, including an adverse horizontal pressure gradient (Figs. 5c,h,m and 6h,m,r) and the presence of KH billows, which have been discussed extensively in the context of SVC formation in this study. The existence of the adverse pressure gradient and the KH billow brings into question the use of ''convergence boundary'' instead of ''gust front'' or ''density current'' per the arguments made in Beck and Weiss (2013). However, since this boundary clearly evolves from a convergence boundary to a density current with time, it does not fit a single classification. We have elected to use ''convergence boundary'' throughout this study due to similar cold pool origins and storm-relative placement as Beck and Weiss (2013).

## 7. Summary and future work

Numerous supercell modeling studies have identified and focused on baroclinic vorticity generation in the forward flank that is streamwise in nature. However, only recently has computing power allowed for finescale investigation, leading to the identification of a region of enhanced horizontal streamwise vorticity called the SVC (Orf et al. 2017). In the present study, CM1 was used to create a high-resolution supercell simulation in which the origin, evolution and structure of the SVC were investigated. Furthermore, high-resolution radar observations have verified the presence and structure of an SVC in two separate nontornadic supercells.

This study has identified the streamwise vorticity current (SVC) as a region of enhanced horizontal streamwise vorticity on the periphery of the forward-flank convergence boundary (FFCB) head in the form of a Kelvin–Helmholtz (KH) billow (located immediately behind the FFCB identified at the surface, Fig. 12a). The mature SVC in this simulation is located between 0.1 and 0.75 km AGL in height (Fig. 12b), extends up to 3 km behind the FFCB (Fig. 12b), and extends along the length of the FFCB between 1 and 10 km (Fig. 12a) upstream of the updraft, depending on the strength of the boundary. While these quantified characteristics are specific to this study, it is reasonable that these values may be applicable to a wide variety of supercells given the FFCB dimensions and placement in other observed supercells (Wakimoto and Liu 1998; Shabbott and Markowski 2006; Wurman et al. 2007; Romine et al. 2008; Frame et al. 2009; Skinner et al. 2011; Kosiba et al. 2013; Skinner et al. 2014; Weiss et al. 2015).

The formation of an SVC is tied specifically to the superposition of the FFCB and the inflow low, allowing Kelvin–Helmholtz instability (KHI) to be released while also axially stretching the associated horizontal vorticity. Thus, the SVCs formation is highly sensitive to storm-scale features. The storm-relative location of the FFCB is not only a function of

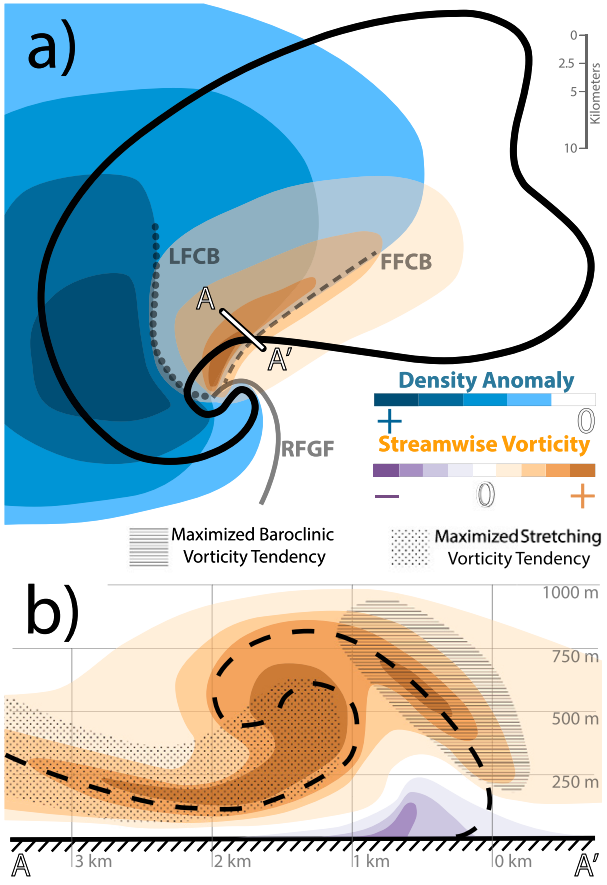


FIG. 12. (a) A plan view conceptual diagram of the FFCB, LFCB, and RFGF placements (black dashed, dotted, and solid lines, respectively) in the supercell as well as their typical respective cold pool magnitudes. The SVC streamwise vorticity magnitude is shown in the orange shades. (b) A vertical cross-sectional conceptual diagram of the FFCB near the updraft, denoted by cross-section AA′ in (a). The black dashed line follows an isentrope as a proxy for the head of the FFCB. The orange (purple) colors represent the placement of positive (negative) streamwise vorticity in the vicinity of the FFCB head. Horizontal hatching delineates the local maximum of baroclinic vorticity generation within the plane, and the stippling delineates the local maximum of stretching within the plane. Approximate height (m AGL) and range levels (km) are shown.

where the precipitation is falling (size sorting), but also a function of precipitation type (microphysical forcing). As the storm matures, the inflow modification may increase and create a stronger cold pool. The strength of the cold pool (density surplus) will depend on the precipitation species, drop size distribution, and subcloud relative humidity. Additionally, the strength of the cold pool, as well as the vertical wind shear strength and direction will affect the storm-relative position and orientation of the boundary. A colder cold pool would be expected to accelerate density current propagation, all else held equal (Simpson and Britter 1980). Conversely, stronger boundary-normal flow opposing the density current propagation may slow the density current down (Simpson and Britter 1980), while stronger boundary-parallel shear may cause the density current to accelerate (Krull 2019). If the position of the boundary is coincident with the inflow low, which depends on vertical wind shear and strength of the updraft (Davies-Jones 2002), maximum horizontal stretching of the vorticity along the density current/convergence boundary will take place; if the FFCB position is outside of the inflow low, the stretching will be reduced and the SVC may not develop. Additionally, if the cold pool is stronger, more vorticity may be generated in the baroclinic regime, and stronger or multiple KH vortices may develop, increasing the vorticity in those regions as well. Future work will address these controls and will attempt to identify characteristics of the environment that lead to SVC formation and strength that may eventually be used in operations. Furthermore, given that this fluid dynamics phenomenon has not yet been addressed in the literature (as far as the authors are aware), numerous research opportunities exist in further analyzing density current dynamics with boundary-parallel flow, and, specifically, boundary-parallel acceleration.

Given that the SVC is partly dependent on density current dynamics, one key limitation of this study is the exclusion of surface friction. Schenkman et al. (2012) attributed the formation of their rotor (containing the same structure and placement as the SVC) to frictional vorticity generation. Roberts et al. (2020) focused on the importance of the inclusion of friction when studying tornadoes in supercell simulations, but noted that the frictional influence was likely dominant in the inflow, which would likely have an impact on the SVC. Given the uncertainty and wide diversity of simulations implementing friction, further research should be done investigating how friction interacts with supercell boundaries and specifically the SVC.

While high-resolution RHIs gathered by the TTUKa radars strongly imply the presence of the SVC and associated KH billow with temporal and spatial coherency, a low-level high-resolution dual-Doppler wind synthesis on a storm that contains an SVC is necessary to capture the full 3D wind and vorticity field, and should be a target of future studies. Operationally, forecasting the potential for an SVC may be fruitful, but observational validation would be necessary to act on imminent threats the SVC may cause. The current WSR-88D network is largely unfit to observe the SVC due to the scanning strategy, large beamwidth, and height of the beam above ground. Dixon (2019) investigated these effects in further detail, and while fortuitous storm-placement relative to the radar may allow a WSR-88D to observe the SVC (their Fig. 15), further research into this topic should be conducted to better identify SVCs using the current infrastructure.

*Acknowledgments.* We thank George Bryan for providing and maintaining the CM1, and the open-source community for providing the Py-ART (Helmus and Collis 2016) and MetPy (May et al. 2008–2020) Python packages used in this analysis. We also thank Erik Rasmussen and Sean Waugh for the observed sounding from the RiVorS project. We acknowledge Eric Bruning for providing helpful insight as a member for the first author's M.S thesis committee. The supercell simulation was

performed at the Texas Tech University High Performance Computing Center (HPCC). Schueth and Weiss are supported by NSF Grants IIS-1527183 and AGS-1824713, and Dahl is supported by AGS-1651786. Finally, we are very grateful for insightful discussions with Kelton Halbert, Jannick Fischer, and Cameron Nixon and the helpful comments provided by Leigh Orf as well as the two anonymous reviewers that improved the quality of this paper.

*Data availability statement.* The dataset on which this paper is based is too large to be retained or publicly archived with available resources. Documentation and methods used to support this study are available at https://github.com/aschueth/research/Schuethetal2021/.

## REFERENCES

Adlerman, E. J., K. K. Droegemeier, and R. Davies-Jones, 1999: A numerical simulation of cyclic mesocyclogenesis. *J. Atmos. Sci.*, **56**, 2045–2069, https://doi.org/10.1175/1520-0469(1999)056<2045:ANSOCM>2.0.CO;2.

Allen, J. R. L., 1985: Loose-boundary hydraulics and fluid mechanics: Selected advances since 1961. *Geol. Soc. London Spec. Publ.*, **18**, 7–28, https://doi.org/10.1144/GSL.SP.1985.018.01.02.

Batchelor, G. K., 1967: *An Introduction to Fluid Dynamics*. Cambridge University Press, 615 pp.

Beck, J., and C. Weiss, 2013: An assessment of low-level baroclinity and vorticity within a simulated supercell. *Mon. Wea. Rev.*, **141**, 649–669, https://doi.org/10.1175/MWR-D-11-00115.1.

Betten, D. P., M. I. Biggerstaff, and C. L. Ziegler, 2018: Three-dimensional storm structure and low-level boundaries at different stages of cyclic mesocyclone evolution in a high-precipitation tornadic supercell. *Adv. Meteor.*, **2018**, 1–24, https://doi.org/10.1155/2018/9432670.

Boyer, C. H., and J. M. L. Dahl, 2020: The mechanisms responsible for large near-surface vertical vorticity within simulated supercells and quasi-linear storms. *Mon. Wea. Rev.*, **148**, 4281–4297, https://doi.org/10.1175/MWR-D-20-0082.1.

Brandes, E. A., 1984: Relationships between radar-derived thermodynamic variables and tornadogenesis. *Mon. Wea. Rev.*, **112**, 1033–1052, https://doi.org/10.1175/1520-0493(1984)112<1033:RBRDTV>2.0.CO;2.

Brown, M., and C. J. Nowotarski, 2019: The influence of lifting condensation level on low-level outflow and rotation in simulated supercell thunderstorms. *J. Atmos. Sci.*, **76**, 1349–1372, https://doi.org/10.1175/JAS-D-18-0216.1.

Bryan, G. H., and J. M. Fritsch, 2002: A benchmark simulation for moist nonhydrostatic numerical models. *Mon. Wea. Rev.*, **130**, 2917–2928, https://doi.org/10.1175/1520-0493(2002)130<2917:ABSFMN>2.0.CO;2.

——, J. C. Wyngaard, and J. M. Fritsch, 2003: Resolution requirements for the simulation of deep moist convection. *Mon. Wea. Rev.*, **131**, 2394–2416, https://doi.org/10.1175/1520-0493(2003)131<2394:RRFTSO>2.0.CO;2.

Buban, M. S., C. L. Ziegler, E. R. Mansell, and Y. P. Richardson, 2012: Simulation of dryline misovortex dynamics and cumulus formation. *Mon. Wea. Rev.*, **140**, 3525–3551, https://doi.org/10.1175/MWR-D-11-00189.1.

Bunkers, M. J., B. A. Klimowski, J. W. Zeitler, R. L. Thompson, and M. L. Weisman, 2000: Predicting supercell motion using a new hodograph technique. *Wea. Forecasting*, **15**, 61–79, https://doi.org/10.1175/1520-0434(2000)015<0061:PSMUAN>2.0.CO;2.

Coffer, B. E., and M. D. Parker, 2017: Simulated supercells in nontornadic and tornadic VORTEX2 environments. *Mon. Wea. Rev.*, **145**, 149–180, https://doi.org/10.1175/MWR-D-16-0226.1.

——, and ——, 2018: Is there a ''tipping point'' between simulated nontornadic and tornadic supercells in VORTEX2 environments? *Mon. Wea. Rev.*, **146**, 2667–2693, https://doi.org/10.1175/MWR-D-18-0050.1.

——, ——, J. M. Dahl, L. J. Wicker, and A. J. Clark, 2017: Volatility of tornadogenesis: An ensemble of simulated nontornadic and tornadic supercells in VORTEX2 environments. *Mon. Wea. Rev.*, **145**, 4605–4625, https://doi.org/10.1175/MWR-D-17-0152.1.

Cohen, R. A., and D. M. Schultz, 2005: Contraction rate and its relationship to frontogenesis, the Lyapunov exponent, fluid trapping, and airstream boundaries. *Mon. Wea. Rev.*, **133**, 1353–1369, https://doi.org/10.1175/MWR2922.1.

Dahl, J. M. L., 2015: Near-ground rotation in simulated supercells: On the robustness of the baroclinic mechanism. *Mon. Wea. Rev.*, **143**, 4929–4942, https://doi.org/10.1175/MWR-D-15-0115.1.

——, 2017: Tilting of horizontal shear vorticity and the development of updraft rotation in supercell thunderstorms. *J. Atmos. Sci.*, **74**, 2997–3020, https://doi.org/10.1175/JAS-D-17-0091.1.

——, M. D. Parker, and L. J. Wicker, 2014: Imported and storm-generated near-ground vertical vorticity in a simulated supercell. *J. Atmos. Sci.*, **71**, 3027–3051, https://doi.org/10.1175/JAS-D-13-0123.1.

Davies-Jones, R., 1982: Observational and theoretical aspects of tornadogenesis. *Intense Atmospheric Vortices*, L. Bengtsson and J. Lighthill, Eds., Springer Berlin Heidelberg, 175–189, https://doi.org/10.1007/978-3-642-81866-0_14.

——, 1984: Streamwise vorticity: The origin of updraft rotation in supercell storms. *J. Atmos. Sci.*, **41**, 2991–3006, https://doi.org/10.1175/1520-0469(1984)041<2991:SVTOOU>2.0.CO;2.

——, 2002: Linear and nonlinear propagation of supercell storms. *J. Atmos. Sci.*, **59**, 3178–3205, https://doi.org/10.1175/1520-0469(2003)059<3178:LANPOS>2.0.CO;2.

——, and H. Brooks, 1993: Mesocyclogenesis from a theoretical perspective. *The Tornado: Its Structure, Dynamics, Prediction, and Hazards*, *Geophys. Monogr.*, Vol. 79, Amer. Geophys. Union, 105–114, https://doi.org/10.1029/GM079p0105.

——, D. W. Burgess, and M. Foster, 1990: Test of helicity as a tornado forecast parameter. *16th Conf. of Severe Local Storms*, Kananaskis Park, AB, Canada, Amer. Meteor. Soc., 588–592.

Dawson, D. T., M. Xue, J. A. Milbrandt, and M. K. Yau, 2010: Comparison of evaporation and cold pool development between single-moment and multimoment bulk microphysics schemes in idealized simulations of tornadic thunderstorms. *Mon. Wea. Rev.*, **138**, 1152–1171, https://doi.org/10.1175/2009MWR2956.1.

Dixon, A., L. Orf, and K. Halbert, 2018: The streamwise vorticity current: Its origin and strategies for remote detection. *29th Conf. on Severe Local Storms*, Stowe, VT, Amer. Meteor. Soc., 84, https://ams.confex.com/ams/29SLS/webprogram/Paper348490.html.

——, 2019: Emulated radar observations of near updraft vorticity in a simulated tornadic supercell. M.S. thesis, Dept. of Atmospheric and Oceanic Science, University of Wisconsin–Madison, 48 pp.

Dowell, D. C., and H. B. Bluestein, 1997: The Arcadia, Oklahoma, storm of 17 May 1981: Analysis of a supercell

during tornadogenesis. *Mon. Wea. Rev.*, **125**, 2562–2582, https://doi.org/10.1175/1520-0493(1997)125<2562:TAOSOM>2.0.CO;2.

——, and ——, 2002a: The 8 June 1995 McLean, Texas, storm. Part I: Observations of cyclic tornadogenesis. *Mon. Wea. Rev.*, **130**, 2626–2648, https://doi.org/10.1175/1520-0493(2002)130<2626:TJMTSP>2.0.CO;2.

——, and ——, 2002b: The 8 June 1995 McLean, Texas, storm. Part II: Cyclic tornado formation, maintenance, and dissipation. *Mon. Wea. Rev.*, **130**, 2649–2670, https://doi.org/10.1175/1520-0493(2002)130<2649:TJMTSP>2.0.CO;2.

Droegemeier, K. K., S. M. Lazarus, and R. Davies-Jones, 1993: The influence of helicity on numerically simulated convective storms. *Mon. Wea. Rev.*, **121**, 2005–2029, https://doi.org/10.1175/1520-0493(1993)121<2005:TIOHON>2.0.CO;2.

Frame, J., P. Markowski, Y. Richardson, J. Straka, and J. Wurman, 2009: Polarimetric and dual-Doppler radar observations of the Lipscomb County, Texas, supercell thunderstorm on 23 May 2002. *Mon. Wea. Rev.*, **137**, 544–561, https://doi.org/10.1175/2008MWR2425.1.

Gilmore, M. S., J. M. Straka, and E. N. Rasmussen, 2004: Precipitation uncertainty due to variations in precipitation particle parameters within a simple microphysics scheme. *Mon. Wea. Rev.*, **132**, 2610–2627, https://doi.org/10.1175/MWR2810.1.

Hane, C. E., and P. S. Ray, 1985: Pressure and buoyancy fields derived from Doppler radar data in a tornadic thunderstorm. *J. Atmos. Sci.*, **42**, 18–35, https://doi.org/10.1175/1520-0469(1985)042<0018:PABFDF>2.0.CO;2.

Helmus, J. J., and S. M. Collis, 2016: The Python ARM Radar Toolkit (Py-ART), a library for working with weather radar data in the Python programming language. *J. Open Res. Software*, **4**, e25, https://doi.org/10.5334/jors.119.

Johns, R. H., J. M. Davies, and P. W. Leftwich, 1993: Some wind and instability parameters associated with strong and violent tornadoes. Part II: Variations in the combinations of wind and instability parameters. *The Tornado: Its Structure, Dynamics, Prediction, and Hazards*, *Geophys. Monogr.*, Vol. 79, Amer. Geophys. Union, 583–590, https://doi.org/10.1029/GM079p0583.

Klemp, J. B., and R. Rotunno, 1983: A study of the tornadic region within a supercell thunderstorm. *J. Atmos. Sci.*, **40**, 359–377, https://doi.org/10.1175/1520-0469(1983)040<0359:ASOTTR>2.0.CO;2.

Kosiba, K., J. Wurman, Y. Richardson, P. Markowski, P. Robinson, and J. Marquis, 2013: Genesis of the Goshen County, Wyoming, tornado on 5 June 2009 during VORTEX2. *Mon. Wea. Rev.*, **141**, 1157–1181, https://doi.org/10.1175/MWR-D-12-00056.1.

Krull, A. J., 2019: The role of boundary-parallel vertical wind shear in convection initiation. M.S. thesis, Dept. of Earth and Atmospheric Sciences, University of Nebraska–Lincoln, 72 pp.

Lee, B. D., and R. B. Wilhelmson, 1997: The numerical simulation of non-supercell tornadogenesis. Part I: Initiation and evolution of pretornadic misocyclone circulations along a dry outflow boundary. *J. Atmos. Sci.*, **54**, 32–60, https://doi.org/10.1175/1520-0469(1997)054<0032:TNSONS>2.0.CO;2.

——, C. A. Finley, and C. D. Karstens, 2012: The Bowdle, South Dakota, cyclic tornadic supercell of 22 May 2010: Surface analysis of rear-flank downdraft evolution and multiple internal surges. *Mon. Wea. Rev.*, **140**, 3419–3441, https://doi.org/10.1175/MWR-D-11-00351.1.

Lerach, D. G., and W. R. Cotton, 2012: Comparing aerosol and low-level moisture influences on supercell tornadogenesis: Three-dimensional idealized simulations. *J. Atmos. Sci.*, **69**, 969–987, https://doi.org/10.1175/JAS-D-11-043.1.

Mallinson, H. M., and S. G. Lasher-Trapp, 2019: An investigation of hydrometeor latent cooling upon convective cold pool formation, sustainment, and properties. *Mon. Wea. Rev.*, **147**, 3205–3222, https://doi.org/10.1175/MWR-D-18-0382.1.

Markowski, P., J. M. Straka, and E. N. Rasmussen, 2002: Direct surface thermodynamic observations within the rear-flank downdrafts of nontornadic and tornadic supercells. *Mon. Wea. Rev.*, **130**, 1692–1721, https://doi.org/10.1175/1520-0493(2002)130<1692:DSTOWT>2.0.CO;2.

——, and Coauthors, 2012: The pretornadic phase of the Goshen County, Wyoming, supercell of 5 June 2009 intercepted by VORTEX2. Part II: Intensification of low-level rotation. *Mon. Wea. Rev.*, **140**, 2916–2938, https://doi.org/10.1175/MWR-D-11-00337.1.

——, Y. Richardson, and G. Bryan, 2014: The origins of vortex sheets in a simulated supercell thunderstorm. *Mon. Wea. Rev.*, **142**, 3944–3954, https://doi.org/10.1175/MWR-D-14-00162.1.

Marquis, J. N., Y. Richardson, P. Markowski, J. Wurman, K. Kosiba, and P. Robinson, 2016: An investigation of the Goshen County, Wyoming, tornadic supercell of 5 June 2009 using EnKF assimilation of mobile mesonet and radar observations collected during VORTEX2. Part II: Mesocyclone-scale processes affecting tornado formation, maintenance, and decay. *Mon. Wea. Rev.*, **144**, 3441–3463, https://doi.org/10.1175/MWR-D-15-0411.1.

May, R. M., S. C. Arms, P. Marsh, E. Bruning, J. R. Leeman, K. Goebbert, J. E. Thielen, and Z. S. Bruick, 2008–2020: Metpy: A python package for meteorological data. Unidata, accessed 22 February 2021, https://doi.org/10.5065/D6WW7G29.

Miles, J. W., and L. N. Howard, 1964: Note on a heterogeneous shear flow. *J. Fluid Mech.*, **20**, 331–336, https://doi.org/10.1017/S0022112064001252.

Morrison, H., G. Thompson, and V. Tatarskii, 2009: Impact of cloud microphysics on the development of trailing stratiform precipitation in a simulated squall line: Comparison of one- and two-moment schemes. *Mon. Wea. Rev.*, **137**, 991–1007, https://doi.org/10.1175/2008MWR2556.1.

Naylor, J., and M. S. Gilmore, 2012: Convective initiation in an idealized cloud model using an updraft nudging technique. *Mon. Wea. Rev.*, **140**, 3699–3705, https://doi.org/10.1175/MWR-D-12-00163.1.

Orf, L., R. Wilhelmson, B. Lee, C. Finley, and A. Houston, 2017: Evolution of a long-track violent tornado within a simulated supercell. *Bull. Amer. Meteor. Soc.*, **98**, 45–68, https://doi.org/10.1175/BAMS-D-15-00073.1.

Prandtl, L., 1953: *Essentials of Fluid Dynamics: With Applications to Hydraulics, Aeronautics, Meteorology and Other Subjets*. Blackie and Son, 452 pp.

Riganti, C. J., and A. L. Houston, 2017: Rear-flank outflow dynamics and thermodynamics in the 10 June 2010 Last Chance, Colorado, supercell. *Mon. Wea. Rev.*, **145**, 2487–2504, https://doi.org/10.1175/MWR-D-16-0128.1.

Roberts, B., M. Xue, and D. T. Dawson, 2020: The effect of surface drag strength on mesocyclone intensification and tornadogenesis in idealized supercell simulations. *J. Atmos. Sci.*, **77**, 1699–1721, https://doi.org/10.1175/JAS-D-19-0109.1.

Romine, G. S., D. W. Burgess, and R. B. Wilhelmson, 2008: A dual-polarization radar-based assessment of the 8 May 2003 Oklahoma City area tornadic supercell. *Mon. Wea. Rev.*, **136**, 2849–2870, https://doi.org/10.1175/2008MWR2330.1.

Rotunno, R., and J. Klemp, 1985: On the rotation and propagation of simulated supercell thunderstorms. *J. Atmos.*

*Sci.*, **42**, 271–292, https://doi.org/10.1175/1520-0469(1985)042<0271:OTRAPO>2.0.CO;2.

Schenkman, A. D., M. Xue, and A. Shapiro, 2012: Tornadogenesis in a simulated mesovortex within a mesoscale convective system. *J. Atmos. Sci.*, **69**, 3372–3390, https://doi.org/10.1175/JAS-D-12-038.1.

Shabbott, C. J., and P. M. Markowski, 2006: Surface in situ observations within the outflow of forward-flank downdrafts of supercell thunderstorms. *Mon. Wea. Rev.*, **134**, 1422–1441, https://doi.org/10.1175/MWR3131.1.

Simpson, J. E., 1972: Effects of the lower boundary on the head of a gravity current. *J. Fluid Mech.*, **53**, 759–768, https://doi.org/10.1017/S0022112072000461.

——, and R. E. Britter, 1980: A laboratory model of an atmospheric mesofront. *Quart. J. Roy. Meteor. Soc.*, **106**, 485–500, https://doi.org/10.1002/qj.49710644907.

Skinner, P. S., C. C. Weiss, J. L. Schroeder, L. J. Wicker, and M. I. Biggerstaff, 2011: Observations of the surface boundary structure within the 23 May 2007 Perryton, Texas, supercell. *Mon. Wea. Rev.*, **139**, 3730–3749, https://doi.org/10.1175/MWR-D-10-05078.1.

——, ——, M. M. French, H. B. Bluestein, P. M. Markowski, and Y. P. Richardson, 2014: VORTEX2 observations of a low-level mesocyclone with multiple internal rear-flank downdraft momentum surges in the 18 May 2010 Dumas, Texas, supercell. *Mon. Wea. Rev.*, **142**, 2935–2960, https://doi.org/10.1175/MWR-D-13-00240.1.

Smagorinsky, J., 1963: General circulation experiments with the primitive equations. *Mon. Wea. Rev.*, **91**, 99–164, https://doi.org/10.1175/1520-0493(1963)091<0099:GCEWTP>2.3.CO;2.

Tanamachi, R. L., L. J. Wicker, D. C. Dowell, H. B. Bluestein, D. T. Dawson, and M. Xue, 2013: EnKF assimilation of high-resolution, mobile Doppler radar data of the 4 May 2007 Greensburg, Kansas, supercell into a numerical cloud model. *Mon. Wea. Rev.*, **141**, 625–648, https://doi.org/10.1175/MWR-D-12-00099.1.

Wakimoto, R. M., and C. Liu, 1998: The Garden City, Kansas, storm during VORTEX 95. Part II: The wall cloud and tornado. *Mon. Wea. Rev.*, **126**, 393–408, https://doi.org/10.1175/1520-0493(1998)126<0393:TGCKSD>2.0.CO;2.

Weckwerth, T. M., and R. M. Wakimoto, 1992: The initiation and organization of convective cells atop a cold-air outflow boundary. *Mon. Wea. Rev.*, **120**, 2169–2187, https://doi.org/10.1175/1520-0493(1992)120<2169:TIAOOC>2.0.CO;2.

Weiss, C. C., J. L. Schroeder, J. Guynes, P. Skinner, and J. Beck, 2009: The TTUKa mobile Doppler radar: Coordinated radar and in situ measurements of supercell thunderstorms during Project VORTEX2. *34th Conf. on Radar Meteorology*, Williamsport, VA, Amer. Meteor. Soc., 11B.2, https://ams.confex.com/ams/34Radar/techprogram/paper_155425.htm.

——, D. C. Dowell, J. L. Schroeder, P. S. Skinner, A. E. Reinhart, P. M. Markowski, and Y. P. Richardson, 2015: A comparison of near-surface buoyancy and baroclinity across three VORTEX2 supercell intercepts. *Mon. Wea. Rev.*, **143**, 2736–2753, https://doi.org/10.1175/MWR-D-14-00307.1.

Weisstein, E. W., 2020: Spherical coordinates. A Wolfram Web Resource. Accessed 22 February 2021, https://mathworld.wolfram.com/SphericalCoordinates.html.

Wicker, L. J., and R. B. Wilhelmson, 1995: Simulation and analysis of tornado development and decay within a three-dimensional supercell thunderstorm. *J. Atmos. Sci.*, **52**, 2675–2703, https://doi.org/10.1175/1520-0469(1995)052<2675:SAAOTD>2.0.CO;2.

——, and W. C. Skamarock, 2002: Time-splitting methods for elastic models using forward time schemes. *Mon. Wea. Rev.*, **130**, 2088–2097, https://doi.org/10.1175/1520-0493(2002)130<2088:TSMFEM>2.0.CO;2.

Wurman, J., Y. Richardson, C. Alexander, S. Weygandt, and P. F. Zhang, 2007: Dual-Doppler and single-Doppler analysis of a tornadic storm undergoing mergers and repeated tornadogenesis. *Mon. Wea. Rev.*, **135**, 736–758, https://doi.org/10.1175/MWR3276.1.